Sensitivity of the Near-Shore Oceanic Circulation Off Central Chile to Coastal Wind Profiles Characteristics

O. Astudillo, B. Dewitte, M. Mallet, J. A. Rutllant, Katerina Goubanova, F. Frappart, M. Ramos, L. Bravo

JGR Oceans

RESEARCH ARTICLE
10.1029/2018JC014051

Sensitivity of the Near-Shore Oceanic Circulation Off Central Chile to Coastal Wind Profiles Characteristics

O. Astudillo[1,2], B. Dewitte[1,2,3,4], M. Mallet[5], J. A. Rutllant[1,6], K. Goubanova[1], F. Frappart[2], M. Ramos[1,3,4,7], and L. Bravo[3,4]

[1]Centro de Estudios Avanzados en Zonas Áridas (CEAZA), La Serena, Chile, [2]Laboratoire d'Etudes en Géophysique et Océanographie Spatiales (LEGOS), Toulouse, France, [3]Departamento de Biología Marina, Facultad de Ciencias del Mar, Universidad Católica del Norte, Coquimbo, Chile, [4]Millennium Nucleus for Ecology and Sustainable Management of Oceanic Islands (ESMOI), Coquimbo, Chile, [5]CNRM UMR 3589, Météo-France/CNRS, Toulouse, France, [6]Departamento de Geofísica, Facultad de Ciencias Físicas y Matemáticas, Universidad de Chile, Santiago, Chile, [7]Centro de Innovación Acuícola Aquapacífico, Universidad Católica del Norte, Coquimbo, Chile

Key Points:
- The characteristics of coastal wind profiles simulated by a regional atmospheric model are sensitive to horizontal resolution
- The onshore wind reduction influences the oceanic circulation in the coastal domain and at regional scale off Central Chile
- The onshore wind reduction influences strongly the balance of processes associated to the maintenance of cool SST along the coast

Correspondence to:
O. Astudillo,
orlando.astudillo@ceaza.cl

Citation:
Astudillo, O., Dewitte, B., Mallet, M., Rutllant, J. A., Goubanova, K., Frappart, F., et al (2019). Sensitivity of the near-shore oceanic circulation off Central Chile to coastal wind profiles characteristics. *Journal of Geophysical Research: Oceans*, *124*, 4644–4676. https://doi.org/10.1029/2018JC014051

Received 5 APR 2018
Accepted 7 JUN 2019
Accepted article online 17 JUN 2019
Published online 9 JUL 2019

Abstract In Eastern Boundary Upwelling Systems (EBUS), the upwelling favorable wind speeds decrease toward the coast in the so-called wind drop-off coastal strip, which has been shown to be influential on the coastal upwelling dynamics, particularly in terms of the relative contributions of Ekman drift and Ekman suction to coastal upwelling. Currently, the wind drop-off length scale is not properly resolved by the atmospheric forcing of regional ocean models in EBUS, featuring a smoother cross-shore wind profile that results in stronger near-shore speeds that could partly explain the coastal cold bias often found in those model simulations. Here, as a case study for the upwelling system off Central Chile, the sensitivity of upwelling dynamics to the coastal wind reduction is investigated using a Regional Ocean Modeling System (ROMS). Coastal wind profiles at different resolutions are first generated using a regional atmospheric model, validated from altimeter data, and then used to correct the coarse atmospheric wind forcing used for sensitivity experiments with ROMS. It is shown that the wind drop-off correction induces a reduction in the oceanic coastal jet intensity, a stronger poleward undercurrent and a coherent offshore Ekman drift. It also yields a significant reduction of the cold bias along the coast compared to the simulation with "uncorrected" winds. Such reduction cannot be solely explained by the reduced Ekman transport only partially compensated by increase in Ekman suction. The analysis of the surface heat budget reveals in fact that an important contributor to the cooling reduction along the coast in the presence of coastal wind drop-off is the heat flux term mediated by the reduction in the mixed-layer depth. Overall, our results illustrate the nonlinear response of the upwelling dynamics to the coastal wind profiles in this region.

1. Introduction

The Humboldt Current System (hereafter HCS) along the coasts of Chile and Peru hosts one of the most productive marine ecosystems of the planet owing primarily to the persistent alongshore winds that drive coastal upwelling conditions through Ekman suction and transport. Strong nearshore equatorward winds favor Ekman divergence at the coast (Halpern, 2002; Rutllant et al., 2004), while the weakening of these alongshore winds toward the shore, known as "wind drop-off" (Capet et al., 2004; Dorman et al., 2006; Perlin et al., 2007; Renault et al., 2012), and the associated cyclonic wind stress curl, favors upward suction of colder waters. While most observational studies of Eastern Boundary Upwelling Systems (hereafter EBUS) have focused on the role of Ekman transport in many aspects of the circulation and ecosystem variability (Carr & Kearns, 2003; Chavez & Messié, 2009; Demarcq, 2009; Wang et al., 2015; among many others), the investigation of the role of Ekman suction on coastal upwelling dynamics has been somehow disregarded owing to limitations in the atmospheric data sets. Not only satellite winds cannot be observed in the coastal fringe (so-called blind zone of ~50-km width) but also atmospheric reanalyses tend to be significantly biased, which in particular consist in an overestimation of nearshore winds (e.g., Astudillo et al., 2017). It is also confusingly assumed in the literature that maximum upward velocity (upwelling) is confined to the coast in a coastal fringe of the size of the local internal Rossby radius of deformation (Croquette et al., 2007; Pickett & Paduan, 2003; Smith, 1995), whereas in fact the cross-shore width of upwelling scales with D/S, the ratio of the Ekman depth layer (D) to the bottom topographic slope (S) (Estrade et al., 2008; see also Capet et al., 2008 for sensitivity experiments to shelf resolution in a regional

model off California). Off Central Chile, characterized by a steep and narrow shelf, this scale cannot be larger than 5 km (Marchesiello & Estrade, 2010), whereas the internal Rossby radius of deformation is around 30 km (Renault et al., 2012). Therefore, mesoscale features in the nearshore winds may be more effective in driving Ekman suction than if only geostrophic adjustment of the upwelling front is assumed.

Since the pioneer modeling studies by Marchesiello et al. (2003) and Capet et al. (2004) that showed that a realistic wind drop-off is influential on the alongshore current dynamics and cross-shore eddy heat fluxes off central California, there has been more concern in the modeling community on the most appropriate wind forcing for regional EBUS modeling studies. While scatterometer winds from QuickSCAT have permitted to produce realistic seasonal oceanic simulations in most EBUS (Aguirre et al., 2012, 2014; Di Lorenzo, 2003; Penven et al., 2001; Penven et al., 2005), a surface cold bias near the coast is usually diagnosed in these simulations (Illig et al., 2014; Penven et al., 2001; Penven et al., 2005; Veitch et al., 2010; O. A. Vergara et al., 2016). As a consequence of this cold bias in regional model simulations of the southern HCS, the equatorward Chile Coastal Current (CCC) is too energetic overlapping and deepening the poleward Peru-Chile Undercurrent (PCU; Aguirre et al., 2012, 2014; Penven et al., 2005; O. Vergara et al., 2017). This results in an enhanced equatorward pressure gradient that forces a shoreward geostrophic current displacing offshore the surface Ekman current. Desbiolles et al. (2016) showed that, for the Benguela upwelling system, this cold bias is associated with an overestimated coastal wind that resulted from an earlier release of the gridded QuickSCAT winds at 0.5° resolution. An updated wind product at 0.25° resolution, using a different quality control has allowed a reduction of the blind zone off the coast to ~12.5 km (Stiles, 2014), reducing therefore the mean cold bias. While part of this bias could be also attributed to a correction of the warm bias in the satellite-based sea surface temperature (SST) data sets (Dufois et al., 2012), current wind products have in any case inherent limitations for accounting for a realistic wind drop-off (Astudillo et al., 2017), which has hampered downstreamed applications, in particular those directed toward marine resources management. This is particularly critical for the coast of Central Chile, which is embedded in an intense oxygen minimum zone that can produce coastal hypoxia depending on environmental conditions (Escribano & Schneider, 2007).

Recently, Astudillo et al. (2017) showed that the wind drop-off takes place all along the coast of the HCS, though with a significant alongshore variability. These mesoscale wind anomalies could respond to physical processes linked to coastal geometry and orography (Pickett & Paduan, 2003; Renault et al., 2015), SST-wind interactions (Boé et al., 2011; Rahn et al., 2011), and sharp changes in surface drag at the sea-land interface (Edwards et al., 2001). As yet few ocean modeling studies have been conducted for the HCS with a high enough horizontal resolution to resolve the mesoscale (i.e., $dx < 10$ km). In addition they have not used a wind forcing (except for case studies) that adequately represents the nearshore wind pattern. Therefore, there is a real need to improve our knowledge of the mesoscale characteristics of the upwelling dynamics and thermodynamics in the HCS and understand how they are linked to the cross-shore wind pattern in order to enhance the ability of regional models to reproduce realistically the observed variability near the coast and thus increase their predictive capability.

Here, we address the issue of the impact of the wind drop-off on the coastal upwelling dynamics for the Central Chile region based on the experimentation with an oceanic regional model. Our focus is on assessing the extent to which the consideration of a wind drop-off in the atmospheric forcing of the regional oceanic model can help in reducing the cold bias usually observed in simulations of the Southern Hemisphere EBUS using scatterometer winds.

The paper is organized as follows: The methodology, experiments' design, and data sets are described in section 2. In section 3, we evaluate the sensitivity of the oceanic circulation off Central Chile to the characteristics of the wind drop-off based on ROMS simulations. Concluding remarks and a discussion are presented in section 4.

2. Data, Model Configurations, and Methodology

2.1. Data

2.1.1. Gridded and Along-Track Satellite Winds

To validate atmospheric model 10-m winds over the HCS, scatterometer Sea Winds aboard the QuikSCAT satellite and the Advanced SCATterometer (ASCAT) aboard Metop-A and Metop-B satellites are used.

Table 1
Description of In Situ Data Sets for Validation

AWS/ADCP	Lat (°S)	Lon(°W)	Elevation (m a.s.l.)	Sensor height (m)	Recording interval (min)	Coast distance (km)	Operation period
Punta de Lobos (CEAZA)	28.29	71.17	22	2.5	10	0.35	2008-7-3 to 2010-2-4
Loma de hueso (CNE)	28.91	71.45	187	10	10	6.5	2006-9-28 to 2009-7-22
Lengua de Vaca (CNE)	30.24	71.62	53	10	10	0.7	2006-9-28 to 2009-7-22
Lengua de Vaca (DGF-CEAZA)	30.25	71.63	10	3.75	30	0.65	1990-3-1 to Present
COSMOS (COPAS)	30.3	71.78	−950	−10 to −110 (each 5 m)	60	13	2003-4-1 to 2006-9-30

Note. The data were provided by the following institutions: Department of Geophysics, Universidad de Chile (DGF), Centro de Estudios Avanzados en Zonas Áridas (CEAZA), National Energy Commission of the Chilean Government (CNE), and Center for Oceanographic Research in the eastern South Pacific (COPAS). Dates are formatted as year-month-day. AWS = Automatic Weather Stations; ADCP = Acoustic Doppler Current Profiler.

The data set consists in the new Level-3 gridded products, containing wind vector fields corresponding to the daily average of both Level-2 swath passes interpolated onto a regular grid of 0.25° in longitude and latitude using an objective method (Bentamy & Fillon, 2012).

However, scatterometer measurements (QuikSCAT and ASCAT) contain a 28- to 50-km-wide blind zone along the coast, limiting the description of the mesoscale atmospheric circulation within this narrow coastal fringe. To overcome this limitation, regional models need to be validated with in situ wind data or high-resolution satellite winds that could be obtained from altimetric measurements (Astudillo et al., 2017). Here we use wind speeds derived from Radar Altimeters at the Ku-band (13.575 GHz) onboard ENVISAT and Jason-1. The surface wind speeds are retrieved using the backscattering coefficient. The accuracy of scatterometer- and altimetry-derived wind products has been determined in several studies using moored buoys and intercomparison, in which the Root Mean Square (RMS) differences did not exceed 2 m/s and 20° for wind speed and direction, respectively, at global and regional scales (Astudillo et al., 2017; Bentamy et al., 2008; Bentamy & Fillon, 2012; Verhoef & Stoffelen, 2013; Vogelzang et al., 2011).

2.1.2. Satellite SST

In this study, we use two satellite-derived SST products: (1) The Operational Sea Surface Temperature and Sea Ice Analysis (OSTIA) is a 5-km gridded global SST product. Data are available from April of 2006 as daily 5-km gridded global SST. More information may be found in Donlon et al. (2012) along with a data description at: http://podaac.jpl.nasa.gov/dataset/UKMO-L4HRfnd-GLOB-OSTIA. (2) The Multi-scale Ultra-high Resolution (MUR) SST analysis is globally gridded at 1-km resolution by merging data from MODIS, AMSR-E, and AVHRR, covering 2002–present. An objective interpolation technique based on a wavelet decomposition (Chin et al., 1998) is used to process each retrieval data set with respect to its inherent resolution. More information and data description can be found at http://podaac.jpl.nasa.gov/dataset/JPL-L4UHfnd-GLOB-MUR and http://mur.jpl.nasa.gov/. The OSTIA product is used to provide the daily SST lower boundary conditions to the regional atmospheric model, whereas the MUR product is used to validate the regional oceanic model SST.

2.1.3. Geostrophic Currents

The altimeter-derived surface geostrophic currents have been used for model evaluation of the surface eddy circulation. These currents were estimated from sea level anomalies for the Globcurrent project (http://globcurrent.ifremer.fr; Rio et al., 2014) and provided by AVISO (Archiving, Validation and Interpretation of Satellite Oceanographic data) with support from the French Space Agency (Centre National d'Etudes Spatiales,). This data set contains absolute geostrophic velocities at 0.25° obtained from merged multisatellite observations (Topex/Poseidon; ERS-2; Jason-1; Envisat) over the Global Ocean.

2.1.4. In Situ Data: Meteo-Oceanographic Buoys

We have considered in situ data to validate the simulated surface winds and the vertical profile of currents near the coast. Table 1 lists the positions, start-end times, and belonging institutions of the four Automatic Weather Stations (AWS) and the mooring COSMOS instrumented with a 300-kHz Acoustic Doppler Current Profiler (ADCP).

2.2. Model Configurations and Methods

Here, we address the wind drop-off issue for the Central Chile region based on the experimentation with both an atmospheric and an oceanic regional model (see domains in Figure 1). The atmospheric model is

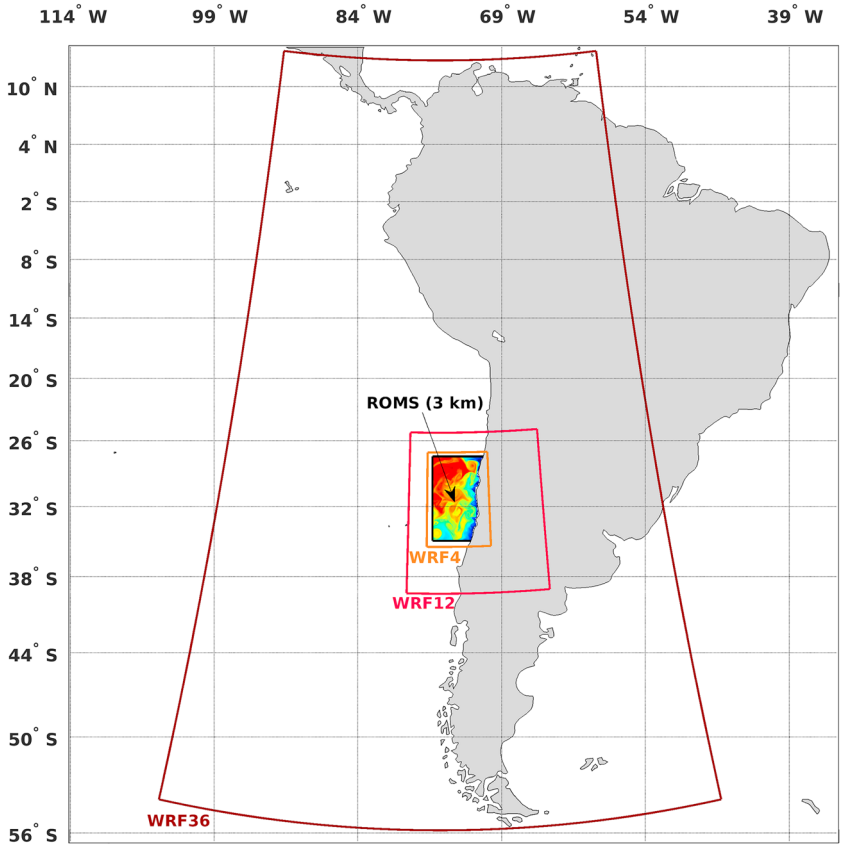

Figure 1. Models domains. The sea surface temperature field represents the Regional Ocean Modeling System (ROMS) inner domain (3 km). The maroon, red, and orange lines delimit the three Weather Research and Forecasting (WRF) domains at 36, 12, and 4 km, respectively.

used to generate atmospheric fields at different resolutions, providing, in particular, coastal wind profiles that are further used to modify the scatterometer-derived winds in the "blind zone" of the satellite. This allows conducting sensitivity experiments with the regional oceanic model in order to isolate the oceanic responses to different wind patterns in the 50-km coastal strip and diagnosing their relationship with the characteristics of the SST bias.

2.2.1. Regional Atmospheric Model Simulations

The Weather Research and Forecasting (WRF) atmospheric model using the Advanced Research WRF solver (Skamarock & Klemp, 2008) has been applied in its 3.5 version. It consists in a fully compressible nonhydrostatic dynamical core with a runtime hydrostatic option on a C-grid with terrain-following mass vertical coordinate. A full suite of parameterization and physics schemes is included in WRF, enabling its use in a broad number of applications allowing for a good resolution of the horizontal scales of the atmospheric mesoscale features involved in Ekman-driven upwelling systems (Boé et al., 2011; Bravo et al., 2016; Oerder et al., 2016; Renault et al., 2012, 2015).

The model was implemented in a multidomain configuration focused on the Central Chile coastal region (26–36°S) including three nests with increasing horizontal grid spacing over the region of interest, corresponding to resolutions of 36, 12, and 4 km, hereafter referred to as WRF36, WRF12, and WRF4, respectively (see Figure 1). The number of vertical sigma levels is 51, with a top at 50 hPa, and stretched resolution toward the surface (~30 m for the surface level). The initial and lateral boundary conditions were derived from the National Centers for Environmental Prediction (NCEP) Final Analysis Data (Kalnay et al., 1996; available online at http://dss.ucar.edu/datasets/ds083. 2/) at 1° × 1° global grid resolution every 6 hr. The SST lower boundary conditions data are based on the daily OSTIA at 0.05° × 0.05° global grid resolution (Stark et al., 2007). The model was run over the period 2007–2009. Model outputs were stored at hourly intervals for each domain resolution. The reader is referred to Bravo et al. (2016) for a detailed description of the

physics parameterizations, whose choice is based on sensitivity tests. The set of parameterizations used in the present study yields the most realistic low-level circulation in the Central Chile region.

As an additional material for assessing the realism of the simulations, we provide in Appendix A the Figures A1 and A2 and the Tables A1 and A2 that compare mean 10-m wind fields and cross-shore 10-m wind speed profiles of the model with estimates from scatterometry, altimetry (Astudillo et al., 2017), and in situ measurements, respectively.

2.2.2. Regional Oceanic Model Simulations

The oceanic simulations were performed with the Regional Ocean Modeling System (ROMS; Shchepetkin & McWilliams, 2005, 2009). ROMS solves the hydrostatic, free-surface primitive equations in 3-D curvilinear coordinates and a stretched terrain-following sigma coordinates, based on the Boussinesq approximation and hydrostatic vertical momentum balance. It has a split-explicit time stepping for the barotropic/baroclinic mode coupling, where short time steps are used to advance the surface elevation and barotropic momentum equations and where a much larger time step is used for temperature, salinity, and baroclinic momentum (Penven et al., 2005). Subgrid-scale vertical mixing is parameterized using the K-Profile Parameterization (KPP) boundary layer scheme (Large et al., 1994). It has been successfully used in previous studies of EBUS (Di Di Lorenzo, 2003; Marchesiello et al., 2003; Capet et al., 2004, 2008; Gruber et al., 2006; Mason et al., 2011; Montes et al., 2010, among many others).

In this study we have implemented a configuration with a domain covering the Central Chile coasts (27–35°S) (Figure 1) at a 3-km (1/36°) horizontal resolution. The domain is slightly smaller than the WRF innermost nest and has 37 vertical σ levels. The bottom topography is derived from the GEBCO 30 arcsec grid data set, interpolated to the model grid and smoothed as in Penven et al. (2005), in order to minimize the pressure gradient errors.

The initial and Open Boundary conditions (OBC) were obtained from a ROMS simulation, which will be referred to hereafter as R-SEP, at ~9-km (1/12°) horizontal resolution used in previous studies of the HCS (Dewitte et al., 2012; O. Vergara et al., 2017). The latter uses the Simple Ocean Data Assimilation Analysis (SODA; Carton & Giese, 2008) as OBCs, and the wind forcing was obtained from the downscaled product NCEP-DS of Goubanova et al. (2011). Atmospheric fluxes (momentum, heat, and freshwater) were derived from the bulk formulas (Fairall et al., 2003) using surface air temperature, precipitation, relative humidity as well as shortwave and longwave radiation fields from COADS 1° monthly climatology (da Silva et al., 1994). This model was run over a domain covering a significant portion of the South-East Pacific (SEP) between 12°N and 40°S so that the dynamics of the PCU is accounted for from its origin near the equator. The reader is invited to refer to Dewitte et al. (2012) and O. Vergara et al. (2017) for assessing the realism of the R-SEP simulation.

The R-SEP 3-day mean outputs are used as OBCs of the model configuration at 1/36°, so that our experimental design consists in a one-way nested domains off-line experiment that takes advantage of the "ROMS2ROMS" downscaling package described in Mason et al. (2010).

The diagnostic simulation (named hereafter CR0) was run over the child domain and uses the same atmospheric forcing as the parent domain bilinearly interpolated on the model grid where data are available (open ocean) and extrapolated in the coastal domain where data are not available. River runoffs were not incorporated for simplicity and because they are thought to have a weak influence on the processes of interest in our regional domain. The model for CR0 was run for the period 2000–2008 with a previous 2-year spin-up repeating the year 2000. CR0 is mostly used here for validation purpose and to assess the realism of the child domain configuration. The reader is invited to refer to Appendix A for assessing the realism of this model configuration.

A series of oceanic model experiments (hereafter named DO36, DO12, and DO4) is then carried out that consist in modifying the characteristics of the nearshore wind forcing (NCEP-DS) so as to mimic the 10-m wind drop-off as simulated by the WRF36, WRF12, and WRF4, respectively. The method for modifying the coastal wind profiles from the WRF outputs is detailed in Appendix B. These experiments consist in simulations over 8 years after a 2-year spin-up during which 3-day averages of the tracer equation terms, as well as model state variables were stored. The simulations consider as forcing the boundary conditions of the year 2008 that is repeated every year. This strategy is chosen so as to ease the interpretation of the results of the sensitivity experiments considering that interannual variability in the region can influence several aspects of the

Table 2
Description of Experiments With the Oceanic Regional Mesoscale Model

Name of the experiment	Period of integration	Lateral boundary conditions (OBC)	Wind forcing	Purpose
CR0	2000–2008 + 2-year spin-up, 3-day average outputs	ROMS R-SEP: 3 days and 9 km of temporal and spatial resolution, over the 2000–2008 period	NCEP-DS: daily forcing and 55 km of spatial resolution,	Validation of the high-resolution model configuration
CR	8 years + 2-year spin-up, 3-day average outputs	ROMS R-SEP: 3-day and 9 km of temporal and spatial resolution, The 2008 OBCs are repeated periodically over 8 years.	NCEP-DS: daily forcing and 55 km of spatial resolution, additionally the 2008 wind forcing is repeated periodically over the 8 years.	Control experiment for assessing the sensitivity's experiments to the cross-shore wind drop-off patterns on upwelling dynamics
DO36	Same as CR	Same as CR	Same as CR. The coastal wind amplitude is modified to mimic the wind drop-off percent as simulated by the 36-km WRF model.	Sensitivity experiment to evaluate the response of the upwelling to a "wide" coastal drop-off.
DO12	Same as CR	Same as CR	Same as CR. The coastal wind amplitude is modified to mimic the wind drop-off percent as simulated by the 12-km WRF model.	Sensitivity experiment to evaluate the response of the upwelling to a "medium" coastal drop-off.
DO4	Same as CR	Same as CR,	Same as CR. The coastal wind amplitude is modified to mimic the wind drop-off percent as simulated by the 4-km WRF model.	Sensitivity experiment to evaluate the response of the upwelling to a "sharp" coastal drop-off.

Note. ROMS = Regional Ocean Modeling System; NCEP = National Centers for Environmental Prediction.

circulation. Additionally, the year 2008 was chosen because its conditions are close to the climatological state in the region of interest (not shown).

As a benchmark for assessing the impact of a wind drop-off in the atmospheric forcing, a control run simulation CR without wind correction is conducted. CR differs from CR0 only in the fact that the year 2008 is repeated in CR while CR0 uses the boundary conditions over the period 2000–008. The different configurations of the oceanic model experiments are summarized in Table 2.

2.3. Methodology

2.3.1. Mixed-Layer Heat Budget

In order to interpret the impact of the change in wind profile on SST along the coast, we compute a mixed-layer heat budget to get insight in potentially important nonlinear processes (i.e., nonlinear advection and mixing) and their sensitivity to wind forcing. This analysis considers the rate of change of the mixed-layer temperature driven by the advection (X-ADV, Y-ADV, Z-ADV), the vertical mixing (vertical diffusion flux V-MIX), and the heat flux (FORC) terms following the equation:

$$\partial_t\langle T\rangle = \underbrace{-\left\langle u\frac{\partial T}{\partial x}\right\rangle}_{X-ADV}\underbrace{-\left\langle v\frac{\partial T}{\partial y}\right\rangle}_{Y-ADV}\underbrace{-\left\langle w\frac{\partial T}{\partial z}\right\rangle}_{Z-ADV} + \underbrace{\left\langle \frac{\partial}{\partial z}\left(K_v\frac{\partial T}{\partial z}\right)\right\rangle}_{V-MIX} + \underbrace{\frac{Q^*}{\rho_w Ch} + \left\langle \frac{Q_s\frac{\partial f(z)}{\partial z}}{\rho_w C}\right\rangle}_{FORC} \quad (1)$$

where T is the model potential temperature within the mixing layer; (u,v,w) are the components of ocean currents; K_v and h are the vertical diffusion coefficient and the mixed-layer depth (MLD) estimated by ROMS KPP scheme; Q_s is the net surface solar heat flux and $f(z)$ is the fraction of the solar radiation that reaches depth z (Paulson & Simpson, 1977), Q^* contains the sum of the other surface heat flux terms, that is, long wave radiation, latent, and sensible heat fluxes. The constants ρ_w and C are the density and the specific heat capacity of seawater respectively. Brackets denote the vertical average over the mixed layer depth: $x = \frac{1}{h}\int_{-h}^{0} x\, dz$. The contributions of the different terms (i.e., FORC, X-ADV, Y-ADV, Z-ADV, and V-MIX) were computed online to ensure a perfect closure of the budget. However, while the tendency terms were calculated online, the vertical averaging and the breakdown of the heat flux forcing term (FORC) were carried out off-line. Note that the temperature tendency term associated with the short wave flux is estimated

here as the difference between FORC and the contributions of the other flux terms. In this way we take into account the effect of the solar penetration within the pycnocline waters.

2.3.2. SST Changes Induced by Ekman Processes

Ekman transport (horizontal advection) and Ekman suction (vertical upward advection) are processes that tend to cool the SST near the coast, which is balanced by the surface heat flux forcing and mixing for the long-term mean and at seasonal time scales. The rate of SST change due to Ekman upwelling writes as follows (notation similar to Hong et al., 2013):

$$\left.\frac{\partial T}{\partial t}\right|_{\mathrm{upw}} = -W_e \frac{\partial T}{\partial z} \tag{2}$$

where T is the temperature, t is time, z is the vertical coordinate, and W_e is the Ekman vertical velocity (units m/s). The vertical gradient of temperature $\frac{\partial T}{\partial z}$ in equation (2) is estimated from the difference of the temperature at the surface and at the base of the mixed layer. The latter value is obtained by linear vertical interpolation to the mixed layer depth (h), estimated by the model from the planetary boundary layer KPP scheme (Large et al., 1994).

The vertical velocity, W_e, at the base of the Ekman layer is due to horizontal divergence or convergence of the Ekman transport (Smith, 1968; Bakun, 1973; Gill, 1982; Halpern, 2002):

$$W_e = \frac{\partial u_e}{\partial x} + \frac{\partial v_e}{\partial y} \tag{3}$$

where u_e and v_e are the zonal and meridional components of the Ekman volume transport (units m^3/s per meter of coast) and defined by Gill (1982) and Pickett and Paduan (2003) as

$$(u_e, v_e) = \frac{1}{\rho_w f}\boldsymbol{\tau}\times\boldsymbol{k} \tag{4}$$

where $\boldsymbol{\tau}$ is the surface wind stress vector computed using the bulk formulations (Fairall et al., 2003), fed with the daily averages of the atmospheric forcing, ρ_w is the density of seawater (assumed constant at 1,024 kg/m^3); f is the Coriolis parameter; and $\boldsymbol{k}$ is the unit vertical vector. Substituting the components of the Ekman transport (4) into equation (3) and computing the Ekman pumping/suction velocity W_e writes as follows:

$$W_e = \frac{\nabla\times\tau}{\rho_w f} + \frac{\beta\tau_x}{\rho_w f^2} \tag{5}$$

where $\nabla \times \tau$ is the wind stress curl calculated using centered derivatives, τ_x is the cross-shore wind stress component, and β is the latitudinal gradient of f along the coast off Central Chile. The second term in (5) is at least 2 orders of magnitude smaller than the first term, so it will be considered negligible.

The horizontal advective heat flux due to the Ekman transport at the surface was computed off-line as follows:

$$Q_{\mathrm{ek}} = \frac{C}{f}\left[-\tau_y \frac{\partial T}{\partial x} + \tau_x \frac{\partial T}{\partial y}\right] \tag{6}$$

where $C = 4{,}185\ \mathrm{J\cdot kg^{-1}\cdot{}^{\circ}C^{-1}}$ is the specific heat capacity of seawater, τ_x and τ_y are the zonal and meridional wind stress, and $\partial T/\partial x$ and $\partial T/\partial y$ are the zonal and meridional SST gradients. The Ekman horizontal velocity is the vertically averaged velocity within the Ekman layer (Yang, 2006):

$$u_{\mathrm{ek}} = \frac{u_e}{h} \tag{7a}$$

$$v_{\mathrm{ek}} = \frac{v_e}{h} \tag{7b}$$

h is the Oceanic Boundary Layer depth, or mixing layer depth, estimated by ROMS (Colas et al., 2012).

The temperature change due to the horizontal advection writes as follows:

$$\left.\frac{\partial T}{\partial t}\right|_{\text{adv}} = -u_{\text{ek}}\frac{\partial T}{\partial x} - v_{\text{ek}}\frac{\partial T}{\partial y} \tag{8}$$

2.3.3. Eddy Kinetic Energy and Eddy Heat flux

In order to assess the effect of the representation of the wind drop-off on some aspects of the eddy field, we first estimate the mean surface Eddy Kinetic Energy (EKE) as

$$EKE = \frac{1}{2}\left(u'^2 + v'^2\right) \tag{9}$$

where u' and v' are the zonal and meridional geostrophic current anomalies, calculated here as the departure from the seasonal mean (i.e., interannual anomalies).

Changes in mean circulation along the coast associated with the wind drop-off have also the potential to change the offshore transport of water mass properties, in particular, its heat content. We will therefore estimate the mean eddy heat flux in the various oceanic simulations, which consists in calculating the covariance between the anomalies in the velocity field and temperature anomalies (Send, 1989). The eddy heat flux vector EH', is defined as

$$EH' = \left(\left\langle u'.T'\right\rangle, \left\langle v'.T'\right\rangle, \left\langle w'.T'\right\rangle\right) \tag{10}$$

where u',v',w', and T' are the zonal, meridional and vertical velocities and temperature anomalies, respectively.

3. Oceanic Model Response

3.1. Impact of the Wind Forcing on Ekman Transport and Ekman Suction

Here, we analyze the linear oceanic response to the various wind profiles. The mean wind stress of the different oceanic simulations is shown in Figure 2. Wind stress is calculated using the COARE algorithm (Fairall et al., 2003). Remember that over the offshore region the wind used to calculate the wind stress is the same in all experiments, whereas within the drop-off length scale the correction described in Appendix B is brought to the NCEP-DS winds to obtain the wind forcing for the drop-off sensitivity experiments. The differences in wind stress along the coast are notorious between experiments ranging from a uniform, wide, medium, and sharp cross-shore wind stress gradient in CR, DO36, DO12, and DO4, respectively (Figures 2a–2d). On average along the coast at the grid point nearest to the coast, the wind stress and wind stress curl (within the 50-km coastal band) reaches 0.0559, 0.0177, 0.0179, and 0.0151 (N/m^2) and -1.4, −6.21, −8.7, and −14.39 (10^{-7} N/m^3) for CR, DO36, DO12, and DO4, respectively. Note that the imposed drop-off does not change the wind stress direction.

From just the wind stress, we can infer the impact on the coastal upwelling dynamics (in the linear sense) through the estimate of Ekman transport and suction. In order to compare both upwelling processes, we had to convert Ekman suction into vertical transport by integrating the vertical velocities (equation (5)) over some offshore distance from the coast, which here corresponds to the maximum value of L_d (50 km) computed along the coast (see Appendix B). In the case of Ekman transport (equation (4)), τ is the wind stress vector at the grid point nearest to the coast. The resulting upwelling estimates, for the different wind drop-off shapes, are displayed in Figures 2e–2g. As expected all the drop-off experiments lead to a reduced (increased) upwelling by Ekman transport (Ekman suction) in relation to the control simulation (see Figures 2e and 2f). However, the increase in upwelling due to Ekman suction does not compensate for the reduction of upwelling due to Ekman transport. Interestingly all the sensitivity experiments exhibits the same upwelling deficit of ~27% as evidenced by Figure 2g that shows the total upwelling by adding the upwelling contribution of Ekman transport and suction for all the experiments.

3.2. SST

While the above analysis indicates substantial impact of the characteristics of the wind drop-off onto the linear Ekman dynamics, we also expect a sensitivity of the mixer-layer thermodynamics (i.e., SST). In this

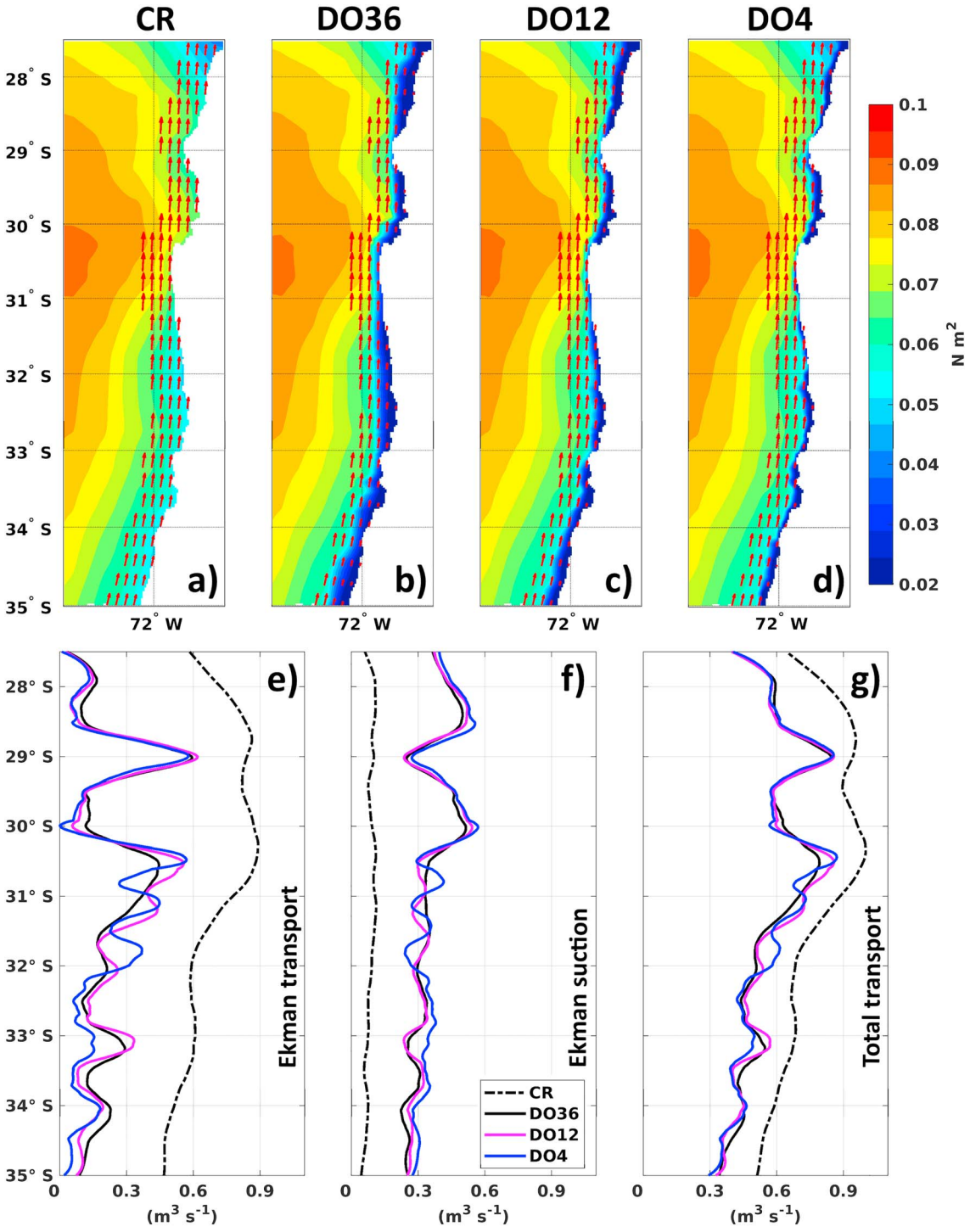

Figure 2. Mean wind stress (N/m^2) field for the various ROMS simulations: (a) CR, (b) DO36, (c) DO12, and (d) DO4. Mean wind stress vectors are displayed for the 50-km coastal band. Note the differences between simulations for the cross-shore wind vectors. Mean upwelling estimates over the simulated period (in m^3/s) as function of latitude for the various ROMS simulations. (e) Horizontal Ekman transport estimated using the wind stress at the grid cell nearest to the coast, (f) vertical transport estimated integrating Ekman suction due to wind stress curl within the 50-km coastal strip, and (g) total upwelling (Ekman transport + Ekman suction). ROMS = Regional Ocean Modeling System.

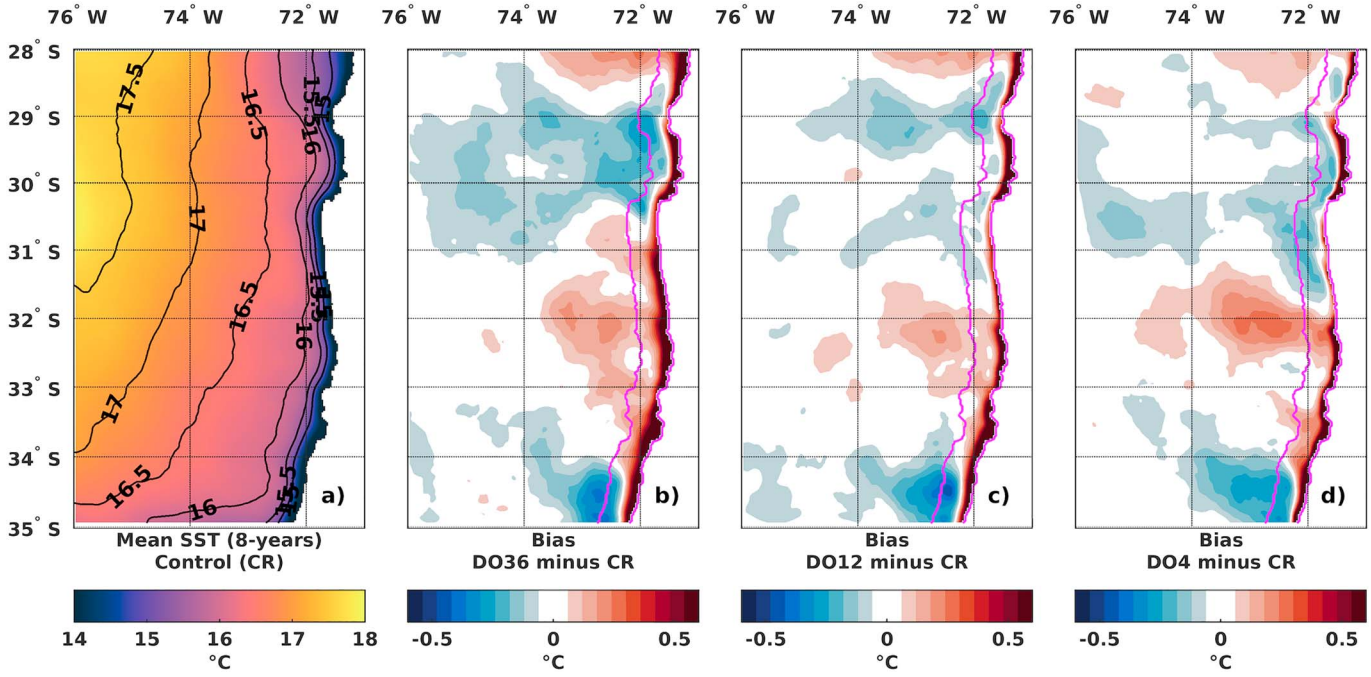

Figure 3. Spatial maps of the (a) Mean SST (°C) simulated by CR. Mean SST bias (°C) for the monthly seasonal differences between (b) DO36, (c) DO12, and (d) DO4 against the reference simulation CR. The lines in magenta indicate the limit of the 50-km coastal band and the shoreline. SST = Sea Surface Temperature.

section we diagnose such impact focusing primarily on how the consideration of a realistic wind drop-off allows reducing the cool mean SST biases along the coast found in our simulation (see section A2.1).

The mean SST in CR (Figure 3a) is shown as a benchmark and exhibits the same biased pattern than in CR0 (see Figure A3), that is, the SST onshore (offshore) is too cold (warm) and the upwelling appears too continuous in the nearshore strip. With regard to the bias reduction, the maps in Figures 3b–3d show the difference between the mean SST of the sensitivity experiments and CR so that the larger the amplitude, the larger the reduction in the cold bias. As we can see, the simulations conducted with corrected wind drop-off lead to a warmer SST along the coast, significantly participating in reducing the cool bias observed in CR. Overall, the comparison between the sensitivity's experiments and the control run, in the 50-km coastal band, indicates an improvement in the realism of the simulation as a function of the resolution: The mean (bias, RMSE) reach (0.23, 0.49), (0.16, 0.41), and (0.13, 0.42) °C for DO36, DO12, and DO4, respectively. Noteworthy, in the simulation DO4, the difference with CR is the lowest closer to the coast than in the other experiments in some regions (e.g., between 31.2°S and 32°S), which indicates that, there, the closer to the coast the wind drop-off starts, the lesser the reduction in the cold bias within the 50-km coastal fringe where most of the cold bias is observed (see Figures 3 and A3). This suggests that in these regions, the DO36 is the most skillful in reducing the cold bias and that the atmospheric simulations at 12 and 4 km tend to yield a wind drop-off too confined to the coast.

Interestingly, besides the coastal zone, the wind drop-off sensitivity differences are also observed in the so-called coastal transition zone, about 100–200 km offshore off Central Chile (e.g., along ~32°S where the wind drop off tends to yield a warm bias). Whether or not this could be associated with differences in eddy activity between CR and the DO experiments will be investigated in section 3.5.

3.3. Alongshore Currents

In order to evaluate the 3-D mean alongshore currents and their dependence on cross-shore winds, we compare the alongshore currents of the sensitivity experiments along four 100-km-long transects across the Central Chile upwelling system. The vertical sections were chosen at latitudes that present a differentiated drop-off scale by experiment (see Figure B2d), while being located near to the main upwelling centers. Figure 4 presents the meridional v component of currents (approximately alongshore) by selected zonal transects for all the experiments. Although the control simulation (CR) shares all the features that appear

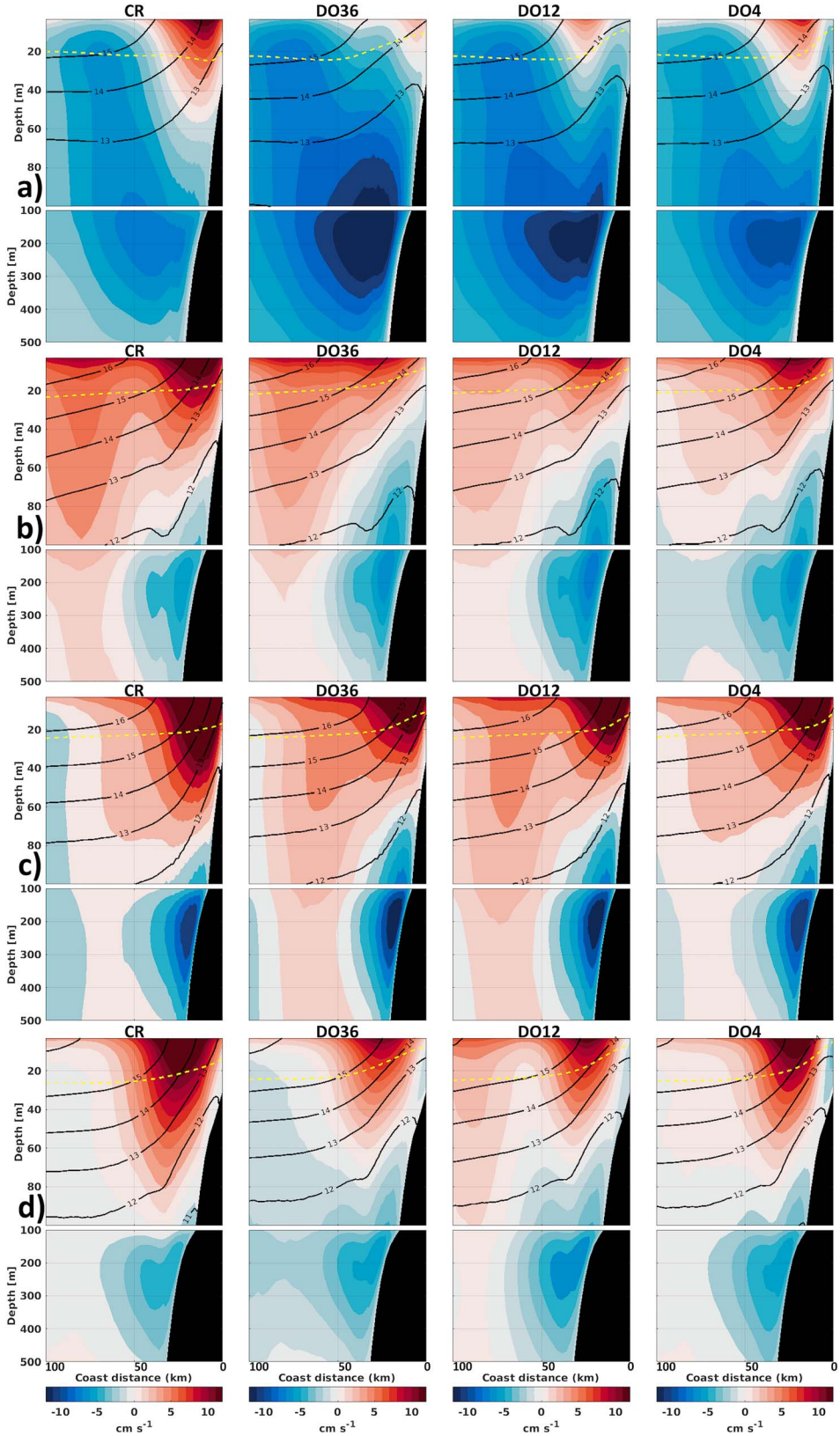

Figure 4. Mean vertical sections of meridional currents for the four experiments at (a) 28.25°S, (b) 30.3°S, (c) 31.1°S, and (d) 33.8°S. Black contours represent the mean temperature, and yellow dashed line is the mean mixed-layer depth diagnosed by K-Profile Parameterization.

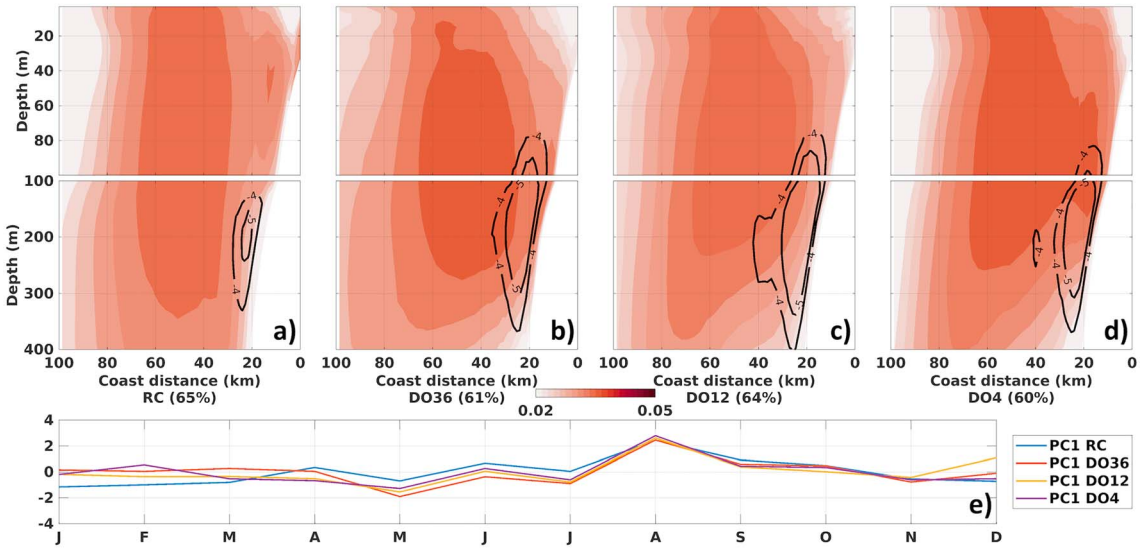

Figure 5. First Empirical Orthogonal Function mode of the meridional current seasonal anomalies (departure from long-term mean) for the vertical sections at 30.3°S for (a) CR, (b) DO36, (c) DO12, and (d) DO4, respectively. The percentage of explained variance is indicated in each panel. The thick black lines superimposed on the contour plot are the −3- and −5-cm/s isolines of the mean meridional current, which indicate the core of the mean Peru-Chile Undercurrent. (e) Corresponding time series (PCs).

in the diagnostic run (see Figure A6b), the sensitivity experiments exhibit naturally a notorious reduction in the CCC (above 60 m) and a stronger alongshore PCU (with the core at approximately 200 m.). As a result, the vertical shear of the alongshore current weakens, the isotherms tilt flattens, and the mixed layer shallows (see yellow dashed lines in Figure 4). Note that the magnitude of these responses is proportional to the resolution of the applied wind drop-off. To assess the realism of the meridional and zonal current structures, we compared them to the ADCP at 30.3°S (see Figure A7 and Table A4). The current profiles are in agreement with previous studies (see Figures 6, 3, and A4 from Aguirre et al., 2012, 2014; O. Vergara et al., 2017). However, the differences between the drop-off experiments and the current observations are reduced by almost 40 % and the correlation levels are increased with respect to the control simulation.

In order to investigate the drop-off impact on the seasonal variability, we use the standard empirical orthogonal function analysis (vonStorch & Zwiers, 1999) to obtain the statistically dominant mode of seasonal variability of the coastal circulation. Figure 5 displays the first mode pattern and its associated temporal expansion (PC1) at 30.3°S. The seasonal cycle (PC1) of the first empirical orthogonal function mode is dominated by an annual cycle component, with a peak centered in August (Figure 5e) and the largest variability at 50 km from the coast. This spatial pattern explains ~60% of the seasonal variance and represents the quasi-barotropic surface equatorward flow linked to the CCC, in connection with the low dynamic heights along the coast resulting from the equatorward winds and offshore Ekman transport (Blanco et al., 2001; O. A. Vergara et al., 2016). The PC1s of the drop-off experiments exhibit increasing correlation against the control solution (CR) depending on drop-off width (0.66, 0.67, and 0.75 for DO36, DO12, and DO4, respectively). The most remarkable drop-off impact in the peak variability pattern is its displacement toward the core of the mean PCU (contours in black lines) that suggests a modulation of the poleward undercurrent absent in CR.

3.4. Mixed-Layer Heat Budget

The contributions of the different processes to the rate of change of the mixed-layer temperature are shown in Figure 6 by spatial maps of the tendency terms along with the mixed-layer depth averaged over 8 years for the simulations CR (top row, Figures 6a–6f) and DO36 (bottom row, Figures 6g–6l). The most striking difference between the two simulations relates to the patterns of the heat-flux forcing term (FORC), which has a much larger amplitude (warming tendency) in the coastal area in DO36 than in CR. This difference can be interpreted as follows: the onshore wide wind drop-off of the DO36 experiment tends to shallow the mixed layer (see Figures 6f and 6l) through the reduction in vertical mixing (i.e., stronger cooling tendency in DO36 associated to the sharper vertical temperature gradient), which overall amplifies the warming tendency due

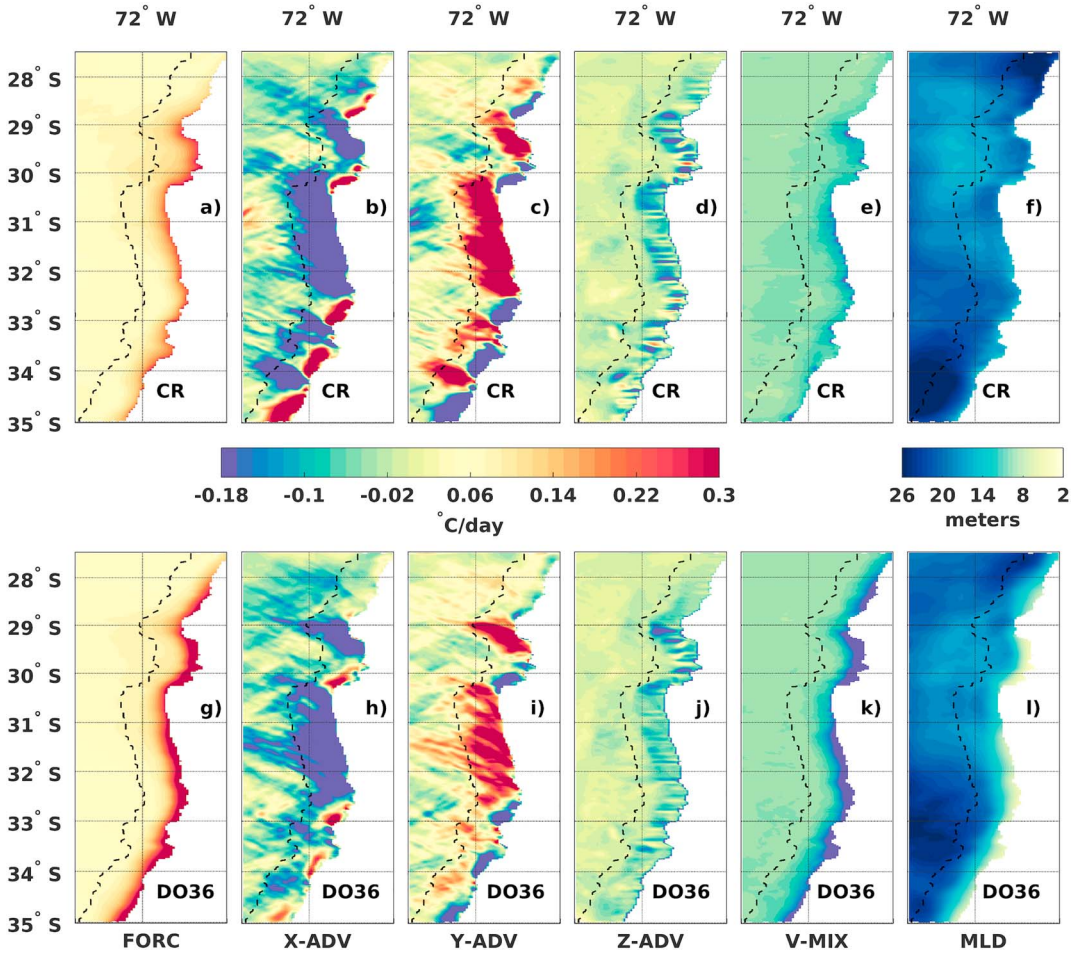

Figure 6. Mixed-layer heat budget analysis: Spatial distribution of the mean tendency terms (°C/day) and the mean mixed-layer depth (m) for the control (CR, top row) and wide drop-off (DO36, bottom row) experiments. (a and g) Heat flux forcing, (b and h) zonal advection, (c and i) meridional advection, (d and j) vertical advection, and (e and k) vertical mixing contributions along the (f and l) mixed-layer depth. The black-segmented line denotes the limit of the 50-km coastal band.

to net heat flux. Most of this increase in warming tendency is associated to change in the solar radiation term, and not to a reduction in the cooling tendency of latent heat flux owing to the reduced coastal winds in DO36. In fact, the weaker onshore winds in DO36 do not lead to a heat gain through reduction of latent heat fluxes, but instead yields a stronger cooling tendency through evaporation and long wave radiation compared to CR because of the warmer mean SST (see Figure 7). Note that such a stronger sensitivity of latent heat to SST than to surface winds was also observed in the modeling study of the Illig et al. (2014) focused on the Peru coastal upwelling. Regarding advection, the differences between CR and D036 are subtler. For vertical advection, in D036, the effect of the shallower mixed layer on the vertical temperature gradient (i.e., increase) compensates for the overall reduction in upwelling rate associated to the reduction in coastal winds compared to CR (see Figure 7). As a result, vertical advection is hardly changed between CR and D036. The patterns of the advection terms are weakly impacted by the changes in the coastal winds (spatial correlation between DO36 and CR reaches at least 0.99 for all the advection terms) and only the amplitude exhibits a notable change, larger in CR than in D036. Vertical and divergent (convergent) zonal advections (Z-ADV and X-ADV in Figures 6d, 6j and 6b, 6h) are contributors to the cooling (warming) tendency in the nearshore zone; on the other hand, meridional advection (Y-ADV in Figures 6c and 6i) is a restoring term and opposes zonal advection.

As a synthetic view of the heat budget in the different simulations, Figure 7 presents the spatial averages (°C/day) within the 50-km coastal strip of the various tendency terms for the control and sensitivity experiments. Focusing first on the cooling terms, Figure 7 indicates that zonal advection is the main contributor to the

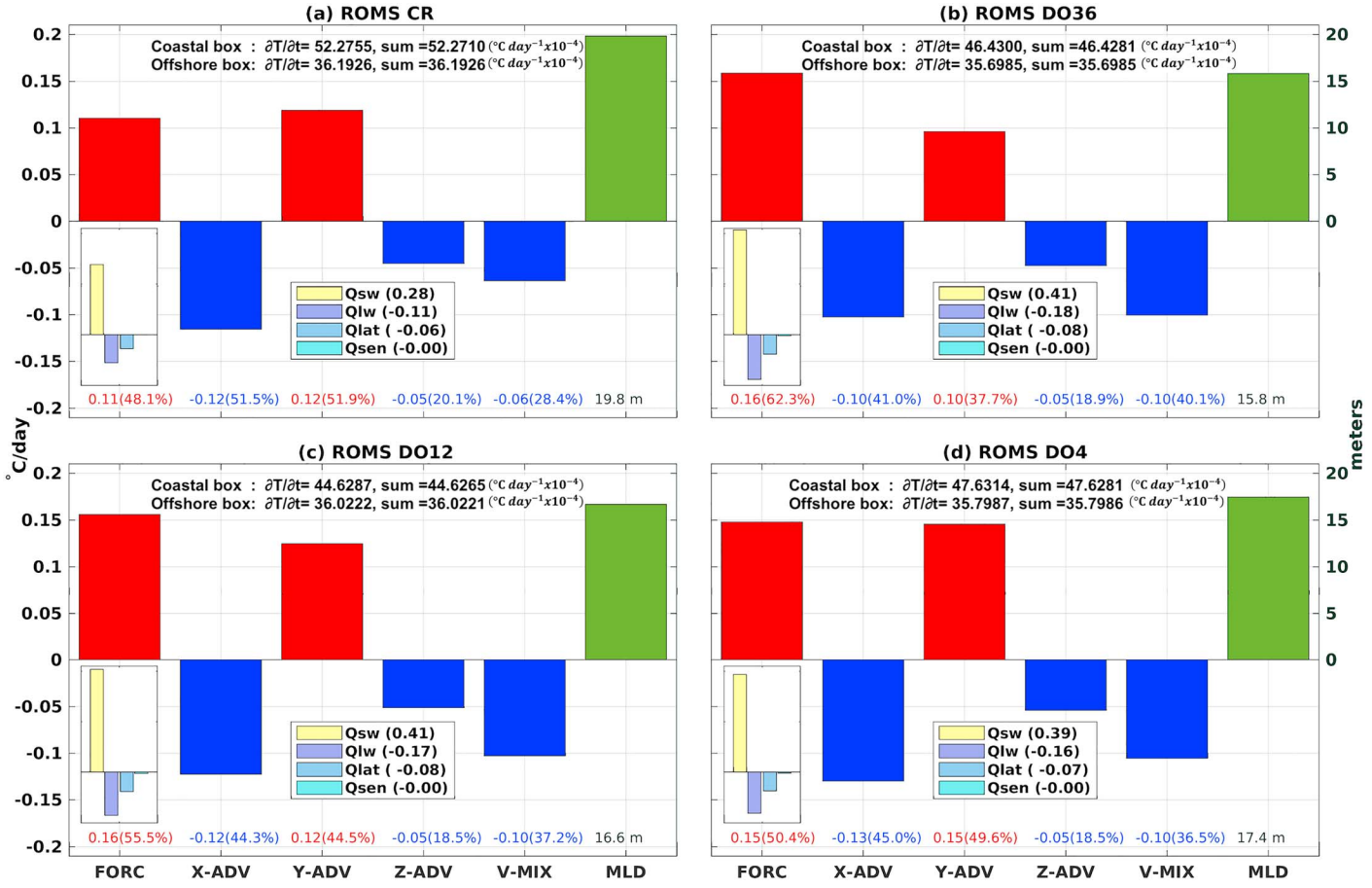

Figure 7. Mixed-layer heat budget analysis in the different simulations: tendency terms averaged over 8 years in the coastal band (50-km wide): (a) CR, (b) DO36, (c) DO12, and (d) DO4. Each bar represents the amplitude of the terms in °C/day (blue (red) for cooling (warming) tendency) and the mixed-layer depth (m). From left to right, heat flux forcing (FORC), zonal advection (X-ADV), meridional advection (Y-ADV), vertical advection (Z-ADV), vertical mixing (V-MIX) and Mixed-Layer Depth (MLD). The percentages of the contribution of the tendency terms to total cooling/warming tendency (in parentheses) are shown at the bottom of each bar. The four components of the net heat flux term are also shown in the rectangle below the FORC bar, with the mean values (in °C/days) indicated in the legend box (yellow = short wave radiation, purple = long wave radiation, blue = latent heat, and light blue = sensible heat). The mean temperature rate and summed-up contributions of the balance are shown for the coastal and offshore box in the upper part of each panel.

coastal cooling in the control simulation, whereas in the sensitivity experiments, both zonal advection and vertical mixing have a comparable contribution (see percentages of the contribution of the tendency term to total tendency at the bottom of each bars in Figure 7), consistent with the coastal wind reduction and the shallower MLD as explained above. The cooling tendency by vertical advection is hardly impacted because of the compensating effect between the reduction in zonal advection and the increase in vertical stratification in the sensitivity experiments. Note the nonlinear response of vertical advection to the changes in the drop-off shape since the vertical advection terms hardly change among the sensitivity experiments despite the notable changes in the coastal wind profiles.

Focusing now on the positive tendency terms (warming tendency), the most notorious impact of the coastal wind reduction is the increase in the contribution of heat flux forcing, which is attributed to the shallower mixed layer in the sensitivity experiment. In particular, the spatially averaged MLD in the 50-km coastal band is on average among the sensitivity experiments shallower by 3.2 m compared to CR (see green bars in Figure 7). The net heat flux term also exhibits structural changes as revealed by the changing relative contribution of solar radiation, long wave flux, sensible heat, and latent heat (see colored thinner bars in the insets of Figure 7). The solar radiation contribution is in particular increased by an average ~45% in all the sensitivity experiments compared to CR as expected by the reduction in the mixed-layer depth. Noteworthy, the cooling tendency associated to latent heat flux is increased in the sensitivity experiments

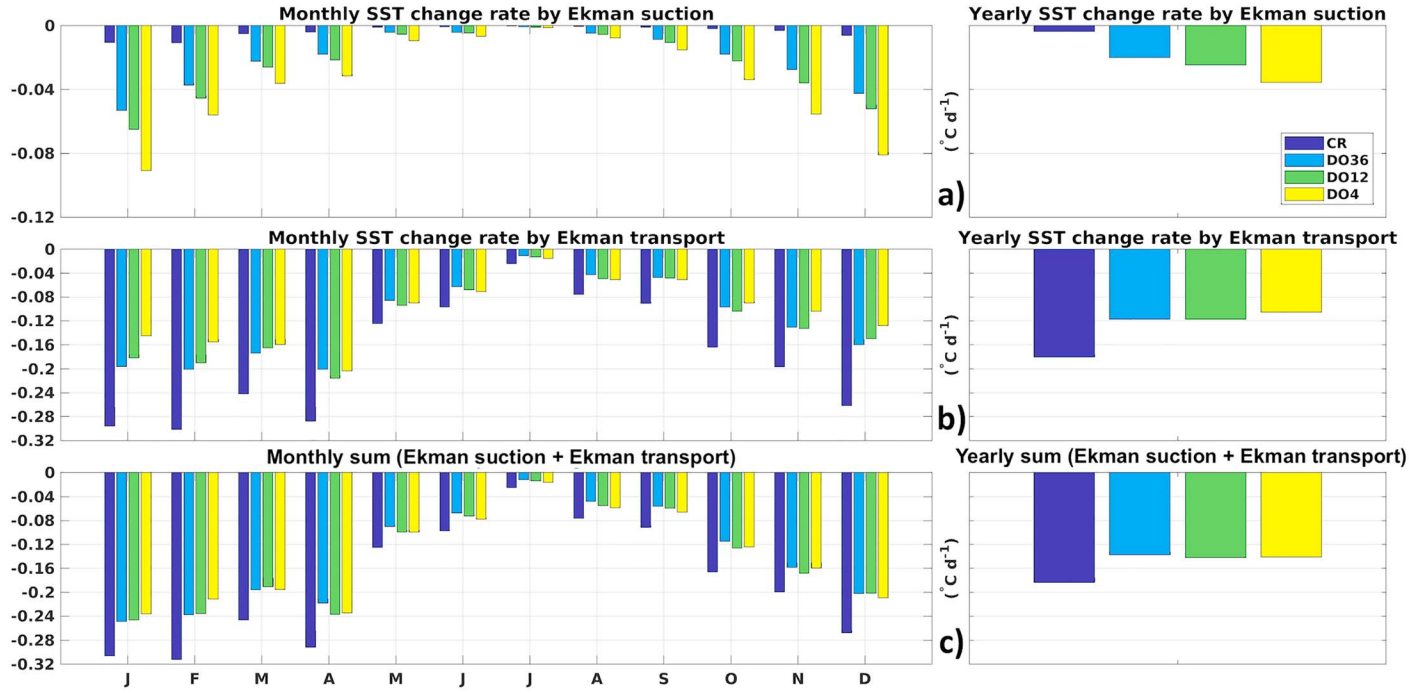

Figure 8. Seasonal variability (left column) and annual mean (right column) of the rate of Sea Surface Temperature (SST) change associated with (a) Ekman suction, (b) Ekman transport, and (c) monthly and yearly sum of Ekman suction and Ekman transport for the various regional oceanic model simulations. Results were spatially averaged over a coastal strip of 50 km and between 27.5 and 35°S (see section 2.3.2 for details of the calculation).

despite the reduction in coastal winds that would tend to reduce cooling through evaporation. However, since the mean SST is warmer in the sensitivity experiments, evaporation and long wave radiation increase, which, added to the effect of the shallower mixed-layer depth, results in an average ~50% increase among the sensitivity experiments of the cooling tendency due to those terms. Meridional advection experiences variations that mirror the ones of zonal advection. Note that although meridional advection decreases in D036 compared to CR, it becomes larger than in CR in D04 despite the presence of a drop-off. Also note that the residual of the heat budget (i.e., difference between the rate of change of the mixed-layer temperature and the sum of all the terms contributing to this tendency) was close to zero (onshore/offshore box (44.69/0.67), (18.94/0.71), (21.61/0.70), (32.17/0.66) (°C/day × 10^{-8}) for CR, DO36, DO12, and DO4, respectively. The analysis thus reveals the nonlinear impact of the drop-off shape on the heat balance and indicates different "regimes" of the maintenance mechanisms of coastal SST depending of the characteristics of the coastal wind profiles. As the most obvious manifestation of such a nonlinear behavior, the FORC term is almost unchanged between the sensitivity experiments while the vertical mixing (and mixed-layer depth) increases strongly from DO36 to DO4. It also indicates that the main impact of the drop-off shape on the thermodynamics in the coastal domain is not through changes in Ekman processes-induced advection but through vertical mixing and heat fluxes, although the reduction in Ekman processes-induced advection is a primarily cause of the warmer SST.

In order to assess the effect of the changes in Ekman processes associated to the different wind profiles on SST along the coast, we follow the approach of Hong et al. (2013) to provide off-line estimates (see section 2.3.2 for details of the calculation) of their relative contributions. The seasonal cycle is considered in the analysis owing to the marked seasonality of the atmospheric circulation off Central Chile, in particular associated to the meridional migration of the low-level jet (Garreaud & Muñoz, 2005; Rahn & Garreaud, 2013; Renault et al., 2012). Figure 8 displays the rate of SST changes (mean and seasonal cycle) associated with advection processes related either to Ekman suction (vertical upward advection) or Ekman transport (horizontal advection). Results were spatially averaged over a coastal strip of 50 km. The mean and seasonal cycle of the SST change rate due to Ekman suction (Figure 8a) exhibit naturally higher amplitude in the drop-off experiments than in CR (mean change rate: −0.0038, −0.0201, −0.0246, and −0.0354

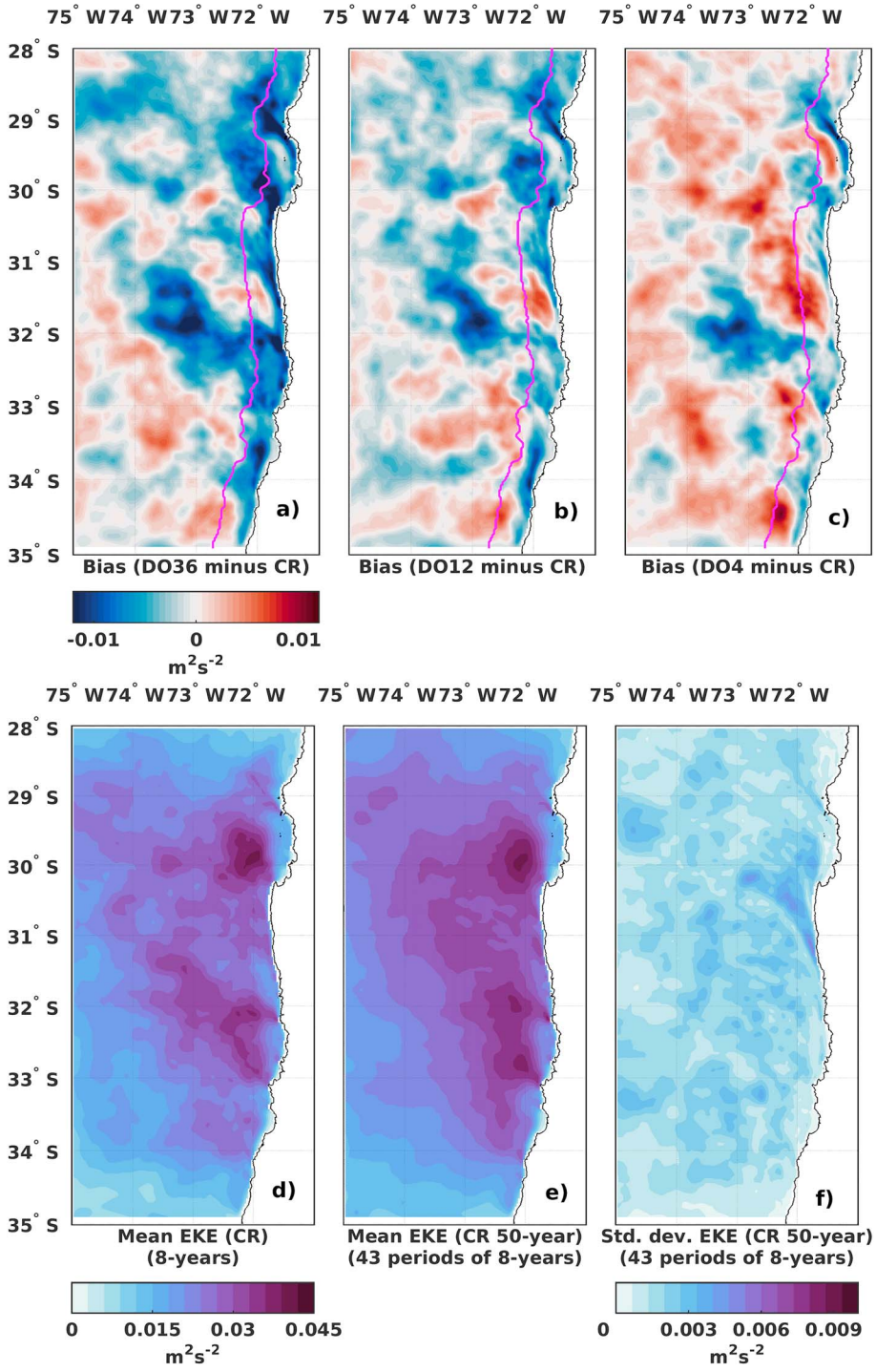

Figure 9. Spatial maps of the temporal mean EKE difference between the control and the drop-off experiments: (a) CR minus DO36, (b) CR minus DO12, and (c) CR minus DO4. (d) Mean geostrophic surface intraseasonal EKE (8 years) simulated by ROMS CR and (e) averaged from 43 chunks of 8 years sampled among a 50-year long simulation with the same characteristics than ROMS CR. (f) Dispersion amongst 43 estimates of mean EKE based on 8-year long chunks selected in the 50-year long simulation. The lines in magenta indicate the limit of the 50-km coastal band. EKE = Eddy Kinetic Energy; ROMS = Regional Ocean Modeling System.

Table 3
Statistics (Mean and Total) of 8-Year Mean Geostrophic Surface Intraseasonal EKE Between Model Solutions

	Onshore EKE (50 km)		Offshore EKE	
Simulation name	Mean (m^2/s^2)	Total (m^2/s^2)	Mean (m^2/s^2)	Total (m^2/s^2)
CR	0.0206	124.1942	0.0190	957.9542
DO36	0.0152	91.7016	0.0172	868.2673
DO12	0.0177	106.8140	0.0176	889.6080
DO4	0.0200	120.4919	0.0195	981.3780

Note. Mean Eddy Kinetic Energy (EKE) values were spatially averaged and integrated in a 50-km coastal band and in the offshore region (i.e., excluding the 50-km coastal strip).

(°C/day) for CR, DO36, DO12, and DO4, respectively). Its magnitude is in phase with the seasonal warming during spring and summer, which increases the vertical gradient of temperature, providing the positive precondition for the surface cooling (Hong et al., 2013). On the other hand, the rate of SST change due to horizontal advection of temperature (Figure 8b) is weaker in the drop-off experiments compared to CR (mean change rate: −0.18, −0.1173, −0.1175, and −0.1053 (°C/day) for CR, DO36, DO12, and DO4, respectively) owing to the reduced coastal divergence in the sensitivity experiments compared to CR. In terms of total temperature change associated with Ekman processes, the main contributor to the cooling is the horizontal advection (Ekman transport) in all simulations, with mean contributions accounting for 98, 85, 83, and 75 (%) of the total contribution by Ekman dynamics for CR, DO36, DO12, and DO4, respectively (see Figure 8). However, all the sensitivity experiments yield a similar reduction (~24%) for the combined contribution of Ekman transport and suction compared to CR, suggesting a compensation between the horizontal and the vertical Ekman advection processes (see Figure 8c).

3.5. Impact on the Turbulent Flow

Since the characteristics of the wind drop-off are influential on the mean circulation along the coast, it is likely to impact the eddy field through changing the stability of the coastal currents. As a first step, we diagnose the impact on EKE. Figure 9 shows the mean EKE for CR (Figure 9d) and its difference with the mean EKE of the three sensitivity experiments (Figures 9a–9c). In the control simulation (CR), the mean EKE amplitude within the 50-km coastal strip (see Table 3) is larger than in all the sensitivity experiments (mean/total EKE 0.0206/124.1942 m^2/s^2), which is not realistic (see Figure A8). The reduction in mean EKE along the coast in the sensitivity experiments can be interpreted as resulting from the reduction of the lateral buoyancy gradient (associated with the reduced cool SST bias), which decreases the available potential energy used by baroclinic instability to produce mesoscale activity along the coast. So near the coast, the impact of the wind drop-off on Ekman dynamics associated to the geostrophic adjustment to the SST front modulating the CCC yields a direct impact on mean EKE. In fact the D036 experiment exhibits the larger reduction in EKE, which means that a wider drop-off implies a lower EKE in the coastal region. Furthermore, the sharper wind drop-off in the D04 simulation compensates the imbalance between the two Ekman processes, and its higher wind stress curl and associated Ekman suction yields the highest EKE amplitude offshore (mean/total EKE 0.0195/981.3780 m^2/s^2). Additionally, we note two regions (around 30°S and 32°) where mean EKE tends to decrease in the presence of a wind drop-off, which corresponds to the regions of largest mean EKE in the control CR simulation.

In order to establish if such changes are significant, we estimate the dispersion in mean EKE expected from random occurrence of eddies. It is estimated based on 43 chunks of 8 years from a 50-year-long simulation corresponding to forcing conditions of CR. The standard deviation among this 43 “virtual” simulations is estimated (Figure 9f) and compared to the change in mean EKE associated with the different sensitivity experiments. It indicates that changes in mean EKE due to changes in the wind profiles near the coasts are much larger than variations in mean EKE associated with different subsampling of the long-term control run experiments. This, in turn, indicates that differences between CR and the sensitivity experiments (Figures 9a–9c) are statistically significant.

To further interpret the impact of the wind drop-off on the eddy field, we estimate the mean zonal and vertical eddy heat flux (see Figure 10) along the same five transects of Figure 4. Generally, eddy advection is contained in the upper pycnocline owing to the small amplitudes of the zonal flow and temperature below ~100 m. The cross-shore lateral flux is essentially shoreward and acts to flatten the upwelling-tilted mean isothermal surfaces (Colas et al., 2012; Gruber et al., 2011; Renault, Deutsch, et al., 2016). The vertical flux is upward and its vertical divergence contributes to the restratification process yielding to the pycnocline in opposition to vertical mixing by boundary layer turbulence. The sensitivity experiments exhibit significant differences in the magnitude and location of the peak value of the mean eddy heat flux, although this is latitudinally dependent. The mean eddy flux of the control experiment (CR) exhibits a lower amplitude than the

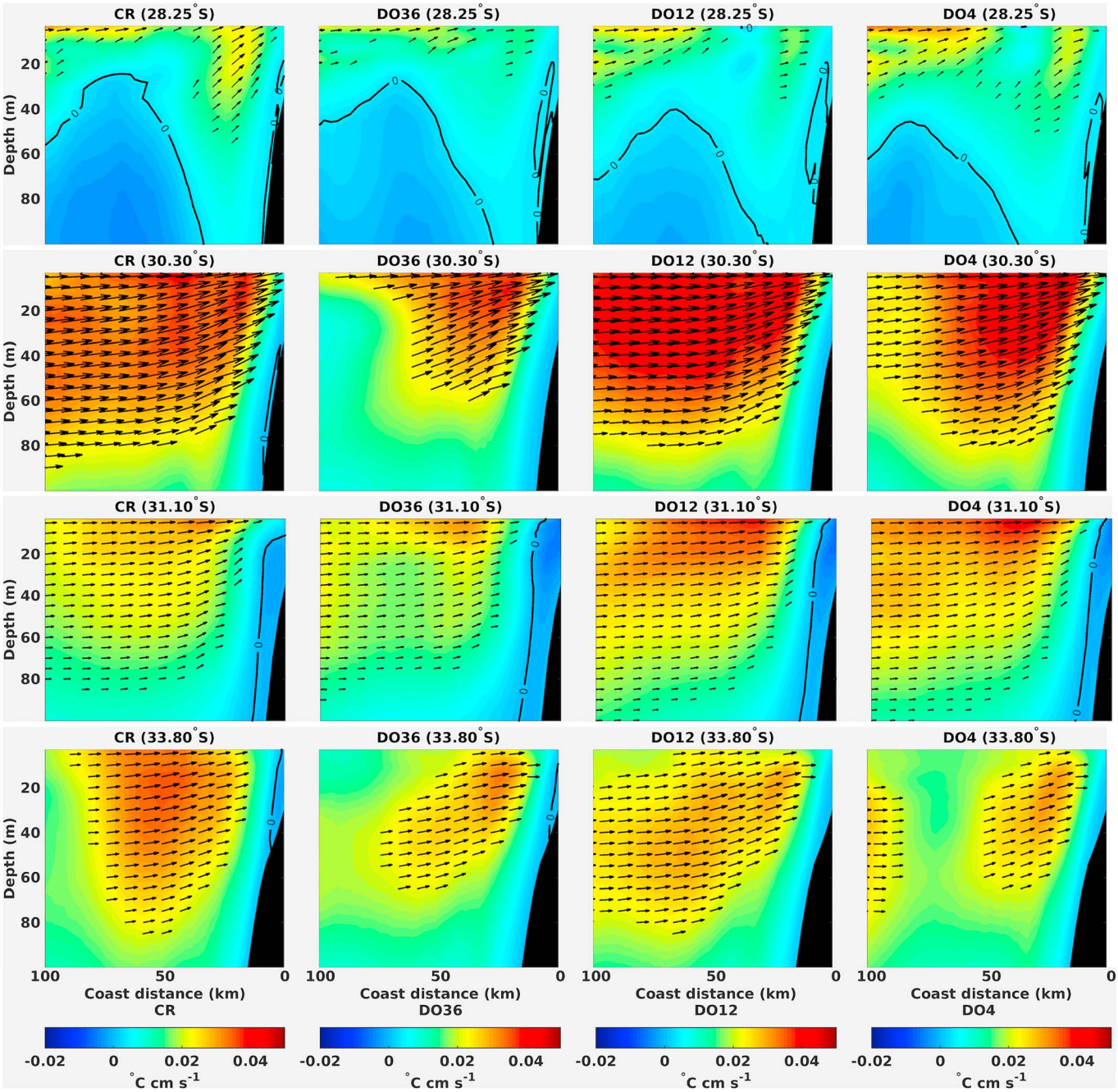

Figure 10. Mean vertical sections of the mean zonal eddy heat flux for the four experiments at (first row) 28.25°S, (second row) 30.3°S, (third row) 31.1°S, and (fourth row) 33.8°S. Black contours represent the 0 flux contour.

experiments forced with a sharp wind reduction (i.e., DO12 and DO4) for all the transects located in the regions where a cool bias was diagnosed near the coast, a sharper drop-off scale leading to a stronger eddy flux. However, the solution DO36 using a wider cross-shore gradient shows lower amplitude than the control experiment revealing the eddy heat flux sensitivity to the drop-off scale. Interestingly, the eddy heat fluxes are lower than in the control solution in all the experiments at the southern transect (33.8°S) where a warm bias was diagnosed in the coastal transition zone for the diagnostic (CR0) and control (CR) experiments.

4. Discussions and Conclusions

Our study was motivated by the need to interpret the coastal cool bias found in most regional model simulations of upwelling system using scatterometer winds that do not represent well the on-shore decrease of the winds in the coastal fringe (the so-called wind drop-off; Astudillo et al., 2017). In this case study focused on the Central Chile region, sensitivity numerical experiments with a regional ocean model to different configurations of the wind forcing were carried out in order to document the influence of mesoscale features in the alongshore winds on the upwelling dynamics. The sensitivity experiments use wind products as simulated by a regional atmospheric model (WRF) at different horizontal resolutions (36, 12, and 4 km) in a nested configuration, which provides a more objective "downscaling" of the wind drop-off pattern on the ocean model grid compared with using the "low" resolution winds (NCEP-DS) as boundary conditions in regional oceanic models.

As a preliminary step we first showed that the regional atmospheric model simulates realistic wind profiles near the coast and that the representation of the wind drop-off is sensitive to the horizontal resolution. In particular the higher the resolution, the closer to the coast the wind drop-off, consistent with previous modeling studies (Capet et al., 2004; Renault et al., 2012). We then performed four cyclic 8-year-long simulations that differ only by the cross-shore profile of the alongshore wind, ranging from a uniform cross-shore gradient to a wide, medium, and sharp drop-off shape.

The experiments reveal a large sensitivity of the thermodynamical processes to the wind drop-off; in particular, there is a notable improvement in the simulated mean SST along the coast. However, a complex balance between various processes governs the reduction of the coastal cold bias. The analysis of a mixed-layer heat budget reveals that vertical mixing is considerably reduced (i.e., its cooling tendency is larger) compared to the case of no wind drop-off. By consequence, the mixed-layer depth shoals, which impacts the amount of heat that is distributed within the mixed layer through surface heat fluxes. In fact, the net heat flux warming tendency is increased by ~45% in all the sensitivity experiments compared to the control run, while there is a weak sensitivity of the change to the resolution of the wind drop-off. Most of this increase in warming tendency is associated to the increase in the solar radiation term. On the other hand, since the mean SST is warmer in the drop-off experiments, cooling by evaporation and long wave radiation increases in ~50% among the sensitivity experiments. What sets these different nonlinear "regimes" of SST maintenance (i.e., with and without drop-off) has its primarily cause in the Ekman processes-induced changes. Indeed, the analysis of the relative contribution of Ekman suction and transport to the rate of SST change for the sensitivity experiments show that the consideration of a drop-off reduces (increases) significantly the cooling by Ekman transport (suction) over the 50-km coastal band. However, the increase in Ekman suction does not compensate for the decrease in Ekman transport, and the resulting cooling rate (i.e., associated to the total upwelling) appears relatively insensitive to the "shape" of the coastal wind profiles. However, the location where the bias reduction takes place varies among the sensitivity experiments. The sharper the drop-off the more confined to the coast the reduction of the cool bias.

In terms of the impact on the upwelling dynamics and associated circulation, the drop-off in the sensitivity experiment has first a profound dynamical impact by reducing the CCC intensity, increasing the alongshore PCU and reducing the offshore Ekman current at the surface with respect to the control run, which yields to a more realistic vertical variability of the coastal currents. Because the eddy field in this region is constrained to a large extent by the baroclinic instability of the coastal current system, the wind drop-off is also influential on the eddy activity. In fact, the sensitivity experiments exhibit significant differences in the magnitude and location of the peak value of the mean eddy heat flux, although this is latitudinally dependent. We also find that the drop-off characteristics influences significantly the EKE field over the whole model domain. In particular, the mean coastal EKE amplitude in the control simulation is larger than in all the sensitivity experiments, and the wide drop-off experiment exhibits the larger reduction in EKE. On the other hand, off shore, EKE tends to decrease in the presence of a wind drop-off. Through the eddy-induced heat transport, such a sensitivity in EKE to the wind drop-off translate into a differentiated flattening of the upwelling-tilted isotherms, which has the potential to feedback on the upwelling dynamics (Gruber et al., 2011).

To conclude, these results illustrate the strong coupling between the wind drop-off and the nonlinear ocean dynamics since the wind drop-off acts not only on all terms of the mixed-layer heat balance but also on the energy source of mesoscale activity through its influence on the vertical structure of the coastal currents.

We will now briefly review limitations of our study. First, the parameterization of the drop-off scale (see Appendix B) proposed here remains mostly empirical, which has inherent limitations. In particular, while we constrain the percentage of decay of the wind amplitude from a certain distance from the coast, there is no constraint imposed on the wind speed at the coast so that, if there is a bias in the offshore wind speed, the parameterization "propagates" it to the coast. Considering the paucity in coastal meteorological stations in this region that would otherwise allow for a better observational constraint, these results can be however considered acceptable. While altimetric data can provide a complementary useful data set to validate the method in the near-coastal region (see Appendix A and Astudillo et al., 2017), they have so far a low latitudinal resolution, which prevents a systematic validation considering that the atmospheric model simulations indicate a large latitudinal variability in the wind drop-off length and the higher-resolution wind forcing does not systematically yield the more realistic reduction of the cool bias evidenced in the control run experiment. This means that other important processes that are not realistically accounted for in our model setup may be at work locally for explaining the discrepancies between model and observations (i.e., cool biases).

One important process is related to atmospheric heat flux forcing. As evidenced by our heat budget analysis, due to the shallow mixed-layer depth near the coast, the annual mean of the rate of temperature change off Central Chile could be strongly influenced by the representation of atmospheric heat fluxes. The oceanic region off Central Chile is, in particular, characterized by the largest stratocumulus cloud deck in the world that exhibits a strong variability from diurnal to interannual scales. Near the coast the variability of low clouds is particularly high and is associated with so-called coastal clearing episodes that accompanied LLCJ and during which incoming solar radiation at sea surface can increase up to 40 W/m^2 (Garreaud & Rutllant, 2003). In our experimental setup that uses the COADS climatological radiative flux forcing (as well as surface air temperature and relative humidity used to calculate turbulent fluxes), these processes may not be properly accounted for, which may partly explain why the sharper drop off (D04) does not yield the largest reduction in the SST cold bias in some regions. Another potentially important process is oceanic mixing (vertical and horizontal diffusivity), which is highly parameterized in the model and thus dependent on model resolution. In particular, the position of the upwelling front is sensitive to where the surface and bottom boundary layers coalesce (Estrade et al., 2008). The reduced winds associated to the drop-off will tend to reduce the thickness of the boundary layer, which will displace the upwelling front further onshoreward, which may explain why in some regions the reduction of the upwelling is insensitive to the resolution of the drop-off. On the other hand, external forcing (internal tides dissipation, inertia-gravity wave, and bores) that will contribute to mixing will have an opposite effect, in particular, in shallow shelf. While the shelf off Central Chile is rather narrow compared to other upwelling systems (i.e., deep shelf), there is thus the possibility of compensating effect between Ekman dynamics and boundary layer dynamics in the positioning of the upwelling front: The sharper the drop-off the more confined the increased upwelling suction but also the thicker the bottom and surface boundary layers through increase in the PCU and surface oceanic jet. Other important processes that may explain the sensitivity of the effect of the drop-off on the reduction cold bias as a function of latitude include the presences of meridional recirculation within the upwelling zone associated to mesoscale dynamics (cf. Capet et al., 2017, for the Southern Senegal upwelling system), the interaction with details in the topography not well accounted for in our configuration, and air-sea coupling at mesoscale (cf. Renault, Molemaker, et al., 2016).

Despite the limitations mentioned above, our results offer a perspective for improving the realism of regional oceanic forced simulations of EBUS in a cost effective way by correcting relatively low resolution wind products, in particular those derived from scatterometers (e.g., QuikSCAT and ASCAT), which are the most used for regional modeling in EBUS. Simply put, we propose here a "cheap" method for correcting satellite winds (or Reanalysis products) to avoid running a fully coupled regional model although the application of this method for other EBUS would require a sensitivity analysis like the one presented here to determine the optimal resolution of the atmospheric model. Here it appears that the DO36 simulation provides the best skill in reducing the average cool bias over the study region.

Future directions of research also include the investigation of the atmospheric processes associated to the wind drop-off so as to better understand the large meridional variability in the sensitivity to the resolution of the model (i.e., the fact that the wind drop-off appears insensitive to resolution in some regions and not in others). While one could follow a similar approach than in Renault et al. (2015) (i.e., vorticity budget and sensitivity experiments to orography), this issue may also require refining topographic features in the

atmospheric model along with resolution, as well as an explicit consideration of air-sea-land coupling (i.e., using a fully coupled ocean-atmospheric regional model), accounting for the potentially important influence of SST on the Marine Boundary Layer at seasonal time scales (Bravo et al., 2016) and at higher frequencies (Garreaud et al., 2011). Local atmospheric processes, as the breeze regime tight to orographic features in the Elqui valley (Scaff et al., 2017) should also be considered.

This study is viewed as a preliminary step for addressing finer-scale variability in the oceanic circulation (i.e., bay's circulation) through downscaling experiments and to guide in the implementation of a regional observing system. In particular, CEAZA is maintaining a dense network of meteorological stations in the Coquimbo region (http://www.ceazamet.cl) and our results could provide guidance for optimizing the network. We are also aiming at carrying specific field campaigns to measure the wind drop-off in some specific regions where the model indicates a weak improvement in the mean coastal SST in order to verify the atmospheric model solution and investigate local effects (e.g., orographic effect, SST coupling). There is also a societal demand for improving the predictive capability of the marine resources and risks/hazards, and we are aiming to build upon this work to investigate some aspects of the biogeochemical response associated to changes in the characteristics of the mesoscale low-level circulation in this region, considering that this region is embedded in one of the largest OMZ of the world and hosts important fisheries. This can be handled with our modeling setup coupling with a biogeochemical model that has been used for the Peru-Chile region to simulate the OMZ seasonal variability (O. Vergara et al., 2016).

Appendix A: Models' Validation

This appendix provides material for the evaluation of the realism of the regional atmospheric and oceanographic model in terms of the mean circulation, seasonal cycle, and mesoscale dynamics. The validation is based on data from satellite, meteorological coastal stations, and a mooring.

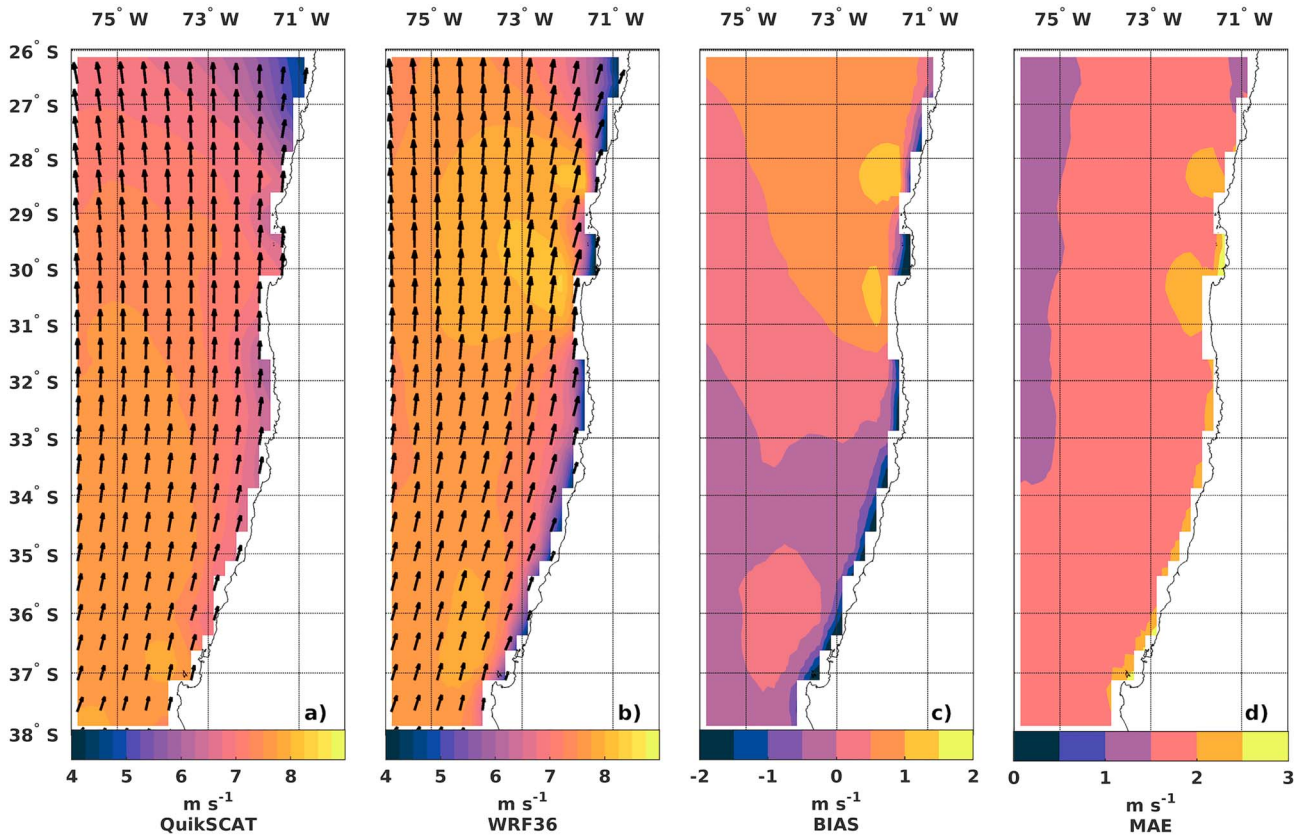

Figure A1. Spatial maps of the temporal mean of the 10-m wind magnitude (m/s) measured by (a) QuikSCAT and simulated by (b) Weather Research and Forecasting (WRF) at coarse resolution 36 km. (c) Bias (m/s) and (d) mean absolute error (MAE, m/s) for the daily differences of the 10-m wind magnitude between WRF and QuikSCAT.

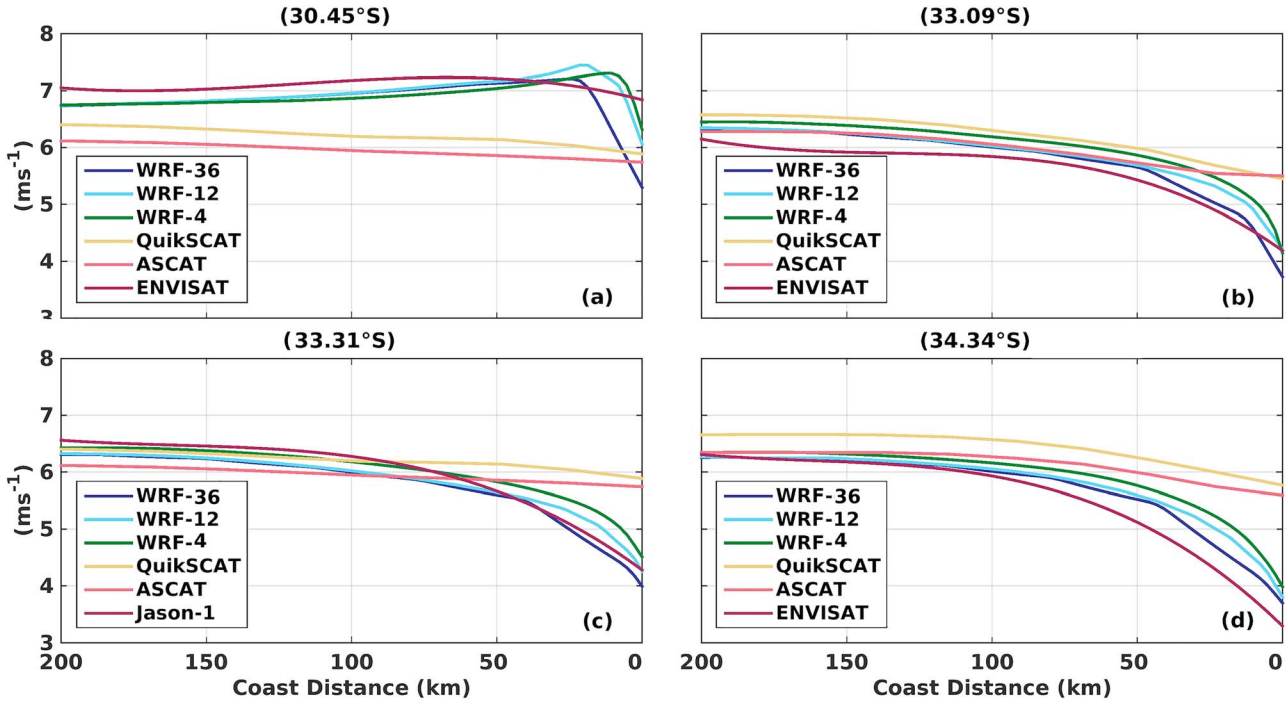

Figure A2. Mean cross-shore 10-m wind speed profiles at different latitudes: (a) 30.45°S, (b) 33.09°S, (c) 33.31°S, and (d) 34.34°S, estimated from WRF36, WRF12, WRF4, QuikSCAT, ASCAT, ENVISAT, and Jason-1 over the period 2007–2009.

Table A1
Summary of the Validation of the WRF Cross-Shore Profiles Using Scatterometers and Altimeters as Ground-Truth Reference (See Figure A2)

		Offshore (80–200 km)				Coast (0–80 km)			
Stat	Resolution	QuikSCAT	ASCAT	Envisat	Jason-1	QuikSCAT	ASCAT	Envisat	Jason-1
ρ	WRF-36	−0.32	−0.34	0.97	0.98	0.64	0.58	0.95	0.99
	WRF-12	−0.31	−0.34	0.97	0.98	0.56	0.51	0.97	0.97
	WRF-4	−0.33	−0.36	0.95	0.98	0.61	0.56	0.97	0.97
RMSE	WRF-36	0.40	0.42	0.20	0.24	1.09	1.04	0.38	0.14
	WRF-12	0.39	0.42	0.21	0.22	0.96	0.93	0.39	0.15
	WRF-4	0.32	0.42	0.30	0.09	0.84	0.84	0.51	0.29
Bias	WRF-36	0.16	0.18	0.04	0.06	1.20	1.09	0.14	0.02
	WRF-12	0.15	0.18	0.04	0.05	0.93	0.87	0.15	0.02
	WRF-4	0.10	0.17	0.09	0.00	0.71	0.70	0.26	0.08

Note. Mean Pearson's correlation coefficient (ρ), Root Mean Square Error (RMSE), and bias are provided. Statistics are obtained at the offshore (80–200 km) and coastal area (0–80 km).

Table A2
Validation Results for WRF (4 km) 10-m Wind Magnitude

Automatic Weather Station (AWS)	Observations (days)	RMSE (m/s)	MAE (m/s)	Bias (m/s)	Pearson's correlation
Punta de Lobos	283	0.5	0.4	0.2	0.8
Loma de hueso	811	1.6	1.3	1	0.8
Lengua de Vaca (CNE)	879	1.6	1.3	0.5	0.7
Lengua de Vaca (DGF)	754	1.9	1.7	1.5	0.8

Note. The analysis uses all available model/AWS daily collocations. Number of daily mean samples, RMSE, MAE, bias and correlation coefficients are shown. WRF = Weather Research and Forecasting; RMSE = Root Mean Square Error error; MAE = Mean Absolute Error; CNE = National Energy Commission of the Chilean Government; DGF = Department of Geophysics, Universidad de Chile.

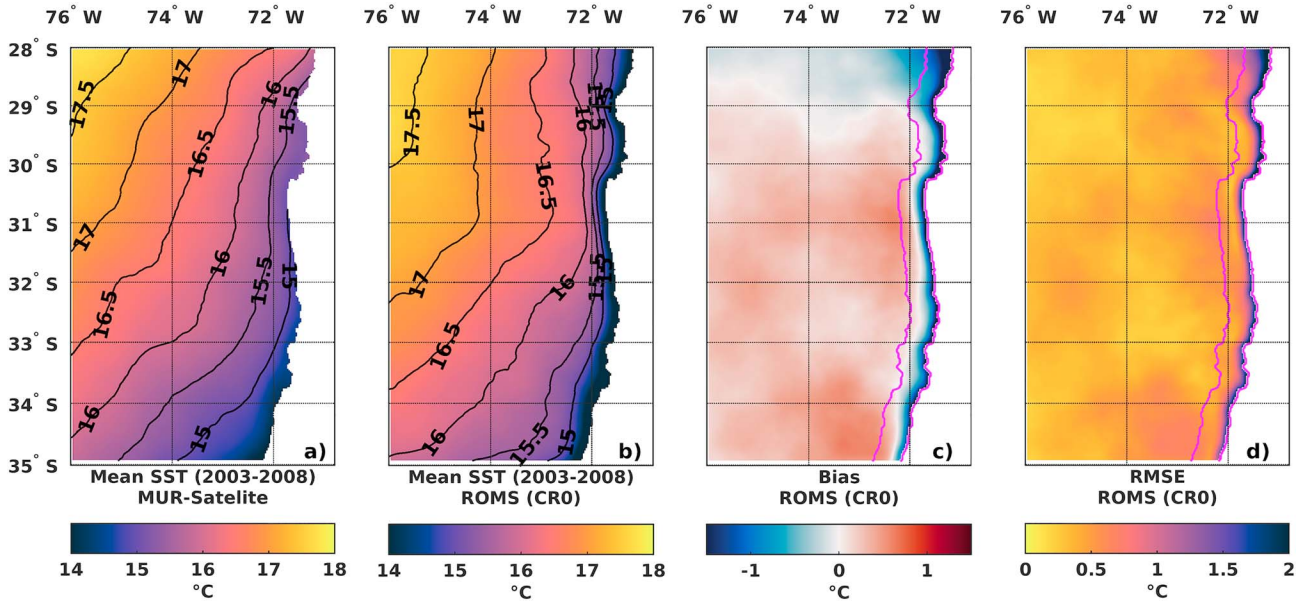

Figure A3. Spatial maps of the temporal mean of the SST (°C) over the period 2003–2008 from (a) MUR data and simulated by (b) ROMS CR0. (c) mean bias (°C), and (d) RMSE (°C) for the monthly seasonal differences between CR and MUR data. The lines in magenta indicate the limit of the 50-km coastal band and the shoreline. SST = Sea Surface Temperature; MUR = Multi-scale Ultra-high Resolution; ROMS = Regional Ocean Modeling System; RMSE = Root Mean Square Error.

A1. Atmospheric Model Evaluation

Figure A1 compares the mean near-surface WRF winds (36-km resolution) with QuikSCAT data over the simulated period (2007–2009) off Central Chile (26–36°S). Observed winds are equatorward and alongshore, with maximum wind magnitude between 30°S and 28°S. In general there is a good agreement between model and observations, both in wind strength and spatial regional patterns. Indeed, the two areas of localized wind speed maxima, the so-called coastal jets (Rahn & Garreaud, 2013), are present in both fields around major capes at Punta Lengua de Vaca (~30°S) and Punta Choros (29°S). However, the wind magnitude appears to be slightly overestimated (~8%) by the model (Figure A1b) in the coastal jet region (Garreaud & Muñoz, 2005). Note that in the nearshore band the model wind strength smoothly decreases shoreward. This wind drop-off is much less pronounced in the scatterometer winds (Figure A1a) as well as in the downscaled wind products used to force CR and CR0 oceanic simulation (not shown). The Figures A1c and A1d display the mean bias and the mean absolute error (MAE) for the daily differences between the model and the QuikSCAT data. Similar results are obtained when comparing WRF and ASCAT winds (not shown), though the agreement between WRF and ASCAT decreases unsurprisingly given that ASCAT has a systematic underestimation of the wind speed that increases with higher wind conditions (Bentamy et al., 2008; Bentamy & Fillon, 2012).

Figure A2 shows the cross-shore profile of the alongshore winds at different latitudes for the three WRF model resolutions and for satellite observations (QuikSCAT, ASCAT, ENVISAT, and Jason-1). First, the simulated WRF winds are comparable with both the scatterometry- and altimetry-derived observations in the offshore region (i.e., excluding the 80-km-width coastal band), with low bias and RMSE differences. Second, in the nearshore region (80 km) the ocean surface winds from WRF agree very well with the altimeter-derived observations and exhibit higher scores with respect to QuikSCAT and ASCAT. This is due to the scatterometer blind zone near the coast, which limit the observation of the wind drop-off profile within this coastal band. On the other hand, the small altimeter footprint and its higher resolution allow resolving the 50-km fringe along the coast. Table A1 provides the validation results for three WRF resolutions.

Finally, the statistics of the mean daily 10-m winds from the WRF innermost solution (4-km resolution) compared to the available coastal surface stations are given in Table A2. The nearshore variability simulated by WRF is in fair agreement with the observations (on average for the four stations, Pearson's correlation is

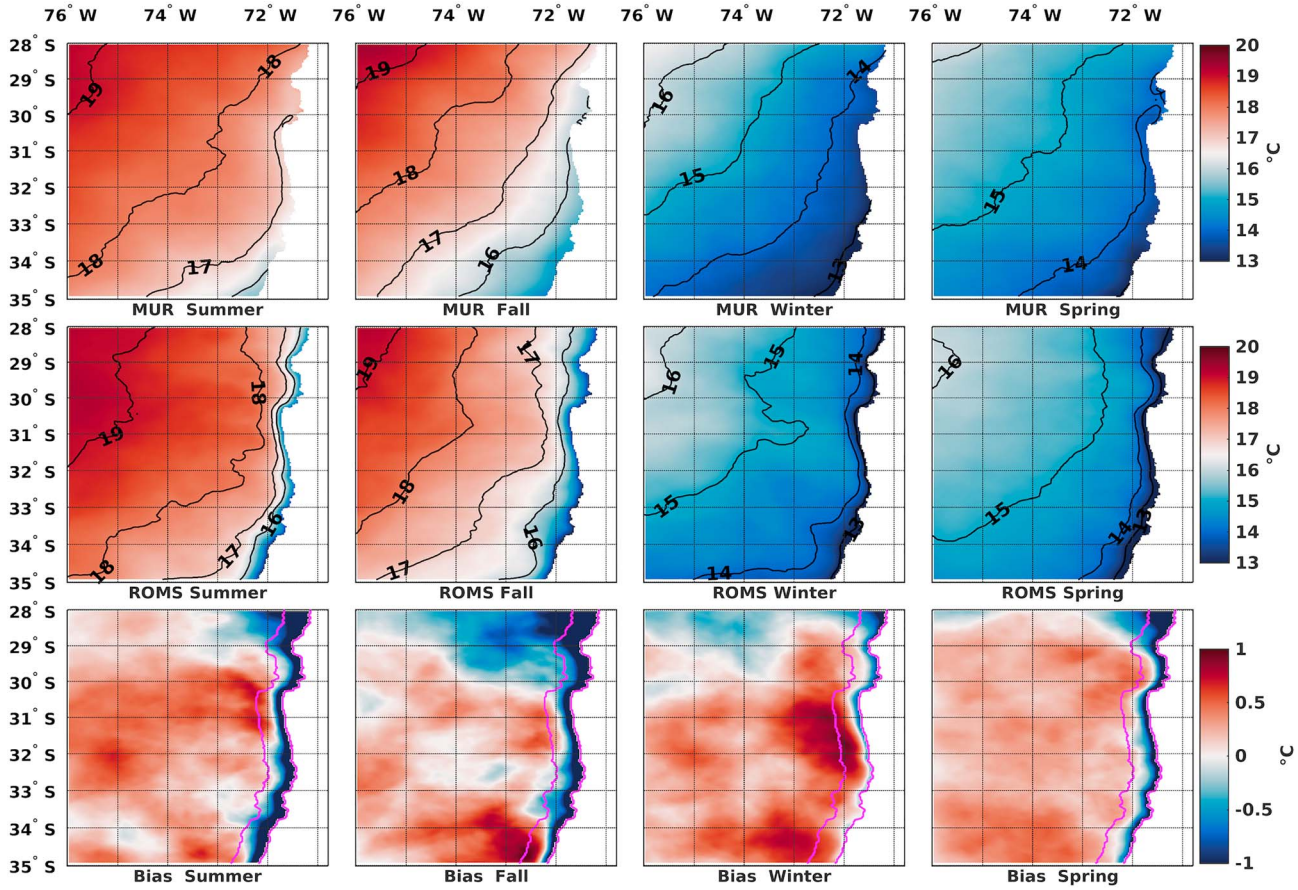

Figure A4. Spatial maps of the temporal mean seasonal of the SST (°C) over the period 2003–2008 from (top row) MUR data and simulated by (middle row) ROMS CR0. (bottom row) Seasonal SST difference between ROMS CR0 and MUR (°C). Summer, fall, winter, and spring are defined as December–February, March–May, June–August, and September–November, respectively. The lines in magenta indicate the limit of the 50-km coastal band and the shoreline. SST = Sea Surface Temperature; MUR = Multi-scale Ultra-high Resolution; ROMS = Regional Ocean Modeling System.

~0.8, bias is ~0.8 m/s, and RMSE is ~1.4 m/s). Note that the anemometer height correction has not been applied on the meteorological records.

A2. Oceanic Model Evaluation

A2.1. SST

In this section, the diagnostic ROMS solution (CR0) is evaluated. The mean state (2003–2008) of observed (MUR) and simulated SST is presented in Figures A3a and A3b. The model mean regional pattern is in good agreement with observations in the offshore region (i.e., excluding the 50-km-width coastal band) and presents a weak positive mean bias and RMSE (0.17 °C and 0.38 °C, respectively). Although both fields exhibit a cold tongue along the coast, clear signature of the wind-driven coastal upwelling, the SST differences (Figures A3c and A3d) for the monthly seasonal cycle indicate that the simulation yields excessive cooling (bias −0.54 °C, RMSE 0.92 °C) in the nearshore strip (50 km). This cold bias extends everywhere along the coast, spreading offshore northwestward off 30°S and upstream from the region of the coastal wind jets shown in Figures A1a and A1b.

In order to analyze in detail this cold bias we describe the seasonal variations of SST for MUR and ROMS CR0 in Figure A4 and Table A3. A pronounced SST seasonal cycle in the upwelling region off Central Chile is

Table A3
Validation of the ROMS SST From the CR0 Simulation Against the Satellite Product (MUR)

Season	Bias (°C) offshore	Bias (°C) coast	RMSE (°C) offshore	RMSE (°C) coast
Summer	0.22	−0.89	0.37	1.07
Fall	0.04	−0.85	0.36	1.09
Winter	0.21	0.06	0.37	0.54
Spring	0.21	−0.47	0.32	0.68
Yearly	0.17	−0.54	0.38	0.92

Note. Mean bias and RMSE are averaged over a 50-km coastal band and in the offshore region (i.e., excluding the 50-km coastal strip) and shown for seasonal and annual means. The months for calculating the seasonal means are defined as in Figure A4. ROMS = Regional Ocean Modeling System; SST = Sea Surface Temperature; MUR = Multi-Scale Ultra-High Resolution; RMSE = Root Mean Square Error.

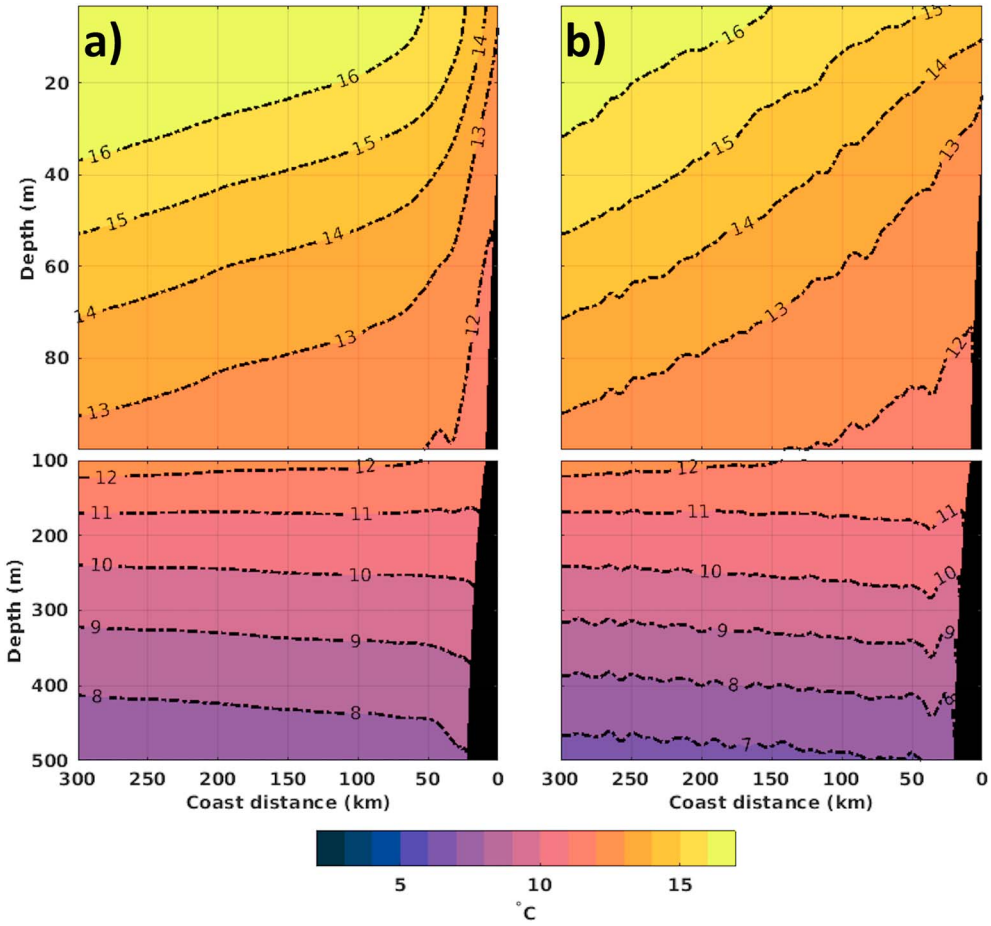

Figure A5. Mean cross-shore vertical sections of temperature at 30.3°S, for the (a) ROMS CR0 simulation and (b) CARS climatology. ROMS = Regional Ocean Modeling System; CARS = CSIRO Atlas of Regional Seas; CSIRO = Commonwealth Scientific and Industrial Research Organisation.

characterized by a westward shift of the 16 °C isotherm from the coast in summer-fall to the offshore region in winter-spring, in both MUR and ROMS (Figure A4, top and middle rows, respectively). The ROMS temperature is slightly warmer offshore (maximum bias 0.22 °C, RMSE 0.37 °C) along the year. On the other hand, the cool bias for the coastal strip evolves in evident relation with seasonal changes in alongshore winds and associated coastal upwelling response; the bias/RMSE in the 50-km coastal band ranges from 0.06/0.54 °C in winter to −0.89/1.07 °C in summer.

The near-coastal cold bias has been present in various regional model simulations of the EBUS (Penven 2001; Penven 2005; Veitch et al., 2010; Colas et al., 2012). In these studies the authors related the cold bias to the wind being too strong at the shore, which results in an imbalance between Ekman transport and Ekman suction (Capet et al., 2004; Desbiolles et al., 2016). However, such a bias could be also attributed to a warm bias in the satellite-based SST data sets. In fact, Dufois et al. (2012) suggest that any high-resolution satellite-derived data set based on a smooth SST product (e.g., MSG/SEVIRI or MODIS L3, or by using optimal interpolation), as MUR analysis, should be used with extreme care in the nearshore regions of the EBUS.

The mean temperature structure is assessed against the CARS climatology (Ridgway et al., 2002). Figure A5 displays a mean zonal section of temperature at 30.3°S for both the CARS climatology and the ROMS CR0. Both sections are in good agreement in the offshore region and in lower layers; however, the surface near-shore cold bias is evident in the sharp isotherm tilt of the model temperature (see Figure A5a).

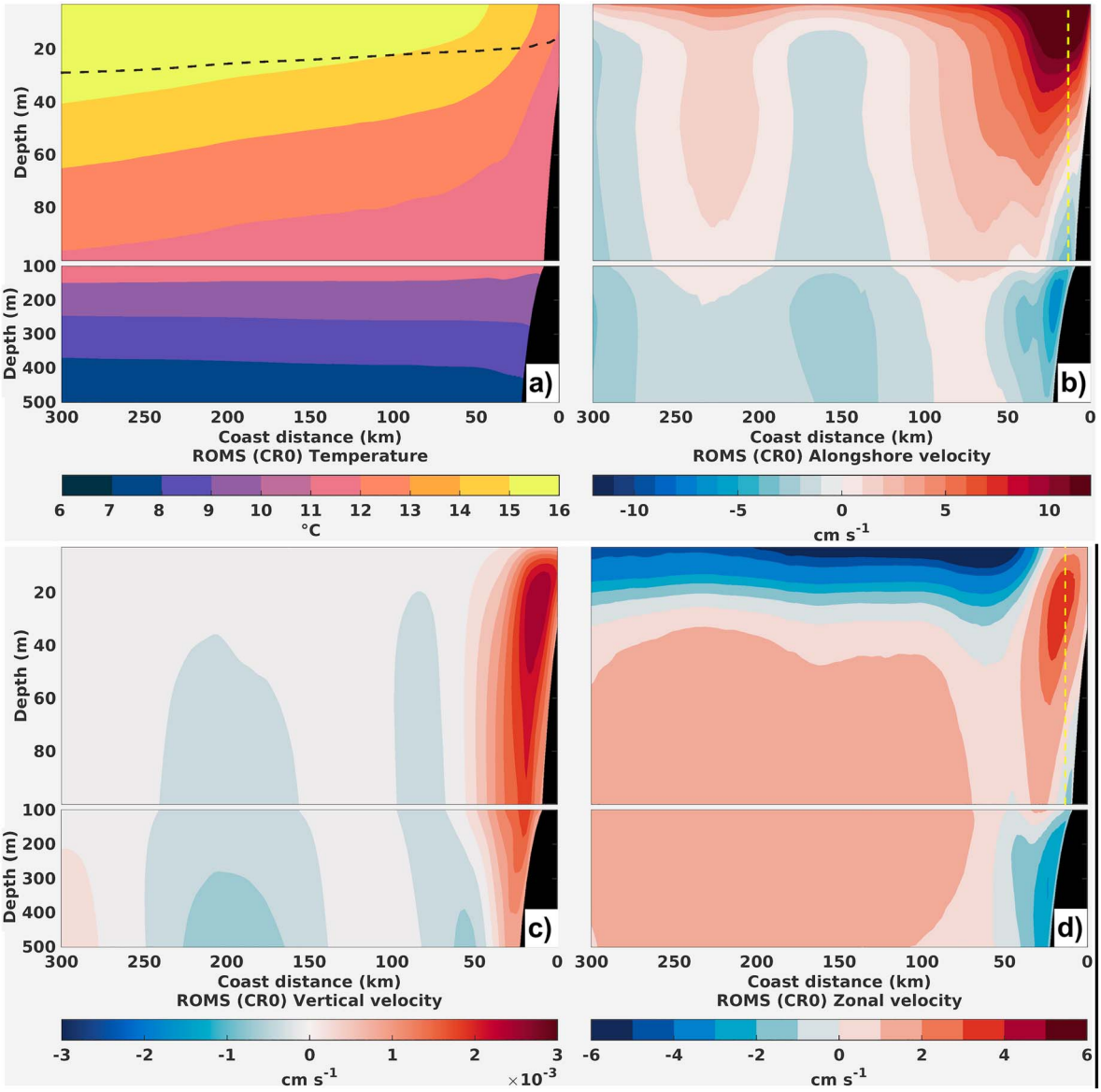

Figure A6. Cross-shore vertical sections at 30.3°S of (a) mean temperature (°C), (b) mean alongshore velocity v (m/s), (c) mean vertical velocity $\overline{w}$ (m/s), and (d) mean zonal velocity $\overline{u}$ (m/s) for the ROMS CR0 model. Dashed lines in black and yellow colors correspond to the mixed-layer depth diagnosed by KPP and to the COSMOS mooring position, respectively. ROMS = Regional Ocean Modeling System; KPP = K-Profile Parameterization.

A2.2. Mean-Seasonal Circulation

The model vertical structure of temperature and currents along a 300-km-long transect at 30°S are presented in Figure A6. Mean alongshore (meridional), cross-shore (zonal), and vertical velocities (Figures A6b–A6d) have the typical structure of a subtropical EBUS and can be compared to previous modeling studies in HCS (Aguirre et al., 2012, 2014; Cambon et al., 2013; O. A. Vergara et al., 2016; O. Vergara et al., 2017). Near the coast the prevalent upwelling conditions associated with the intense and uniform alongshore wind stress cause a surface (above a depth of 50 m) coastal jet, called CCC (mean speed of 20 cm/s) flowing toward the equator, above a subsurface poleward flow (PCU) trapped to the continental slope. This undercurrent exhibits a maximum speed core at about 150- to 300-m depth and originates from the Equatorial Undercurrent, which splits at the Galapagos Islands. One branch continues as undercurrent and turns south to form this subsurface flow. While the other southern branch, the Peru-Chile Countercurrent, at about 150 km from the coast, generates a second southward surface flow (Penven et al., 2005). Finally, farther offshore the eastern branch of the subtropical South Pacific gyre gives raise to another wind-driven equatorward

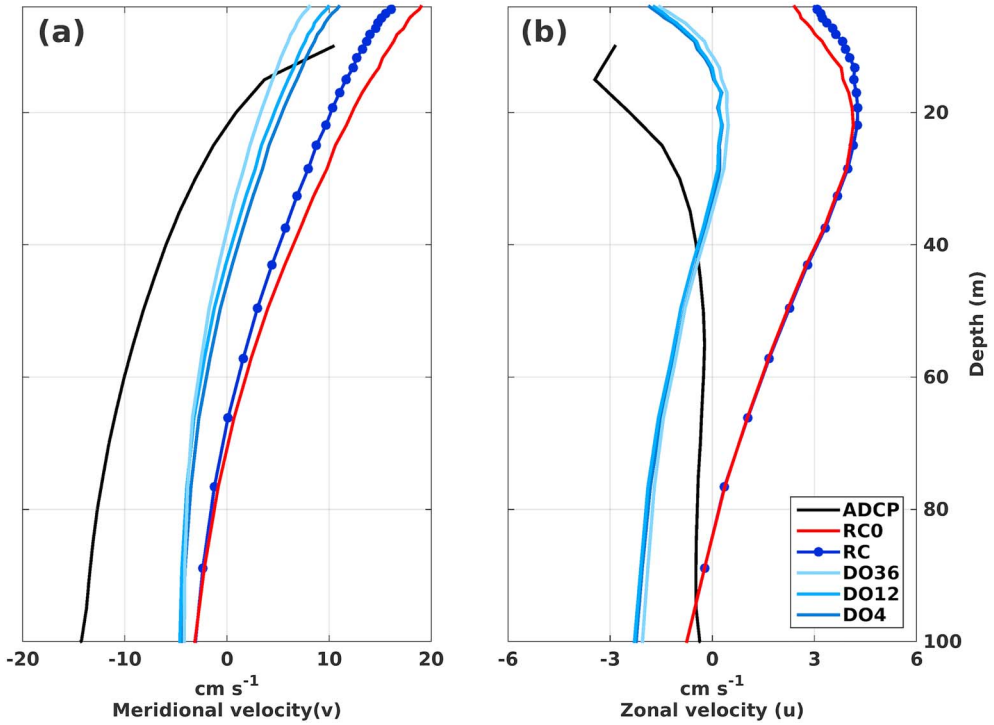

Figure A7. (a) Mean meridional and (b) zonal current profiles at 30.3°S from the COSMOS Acoustic Doppler Current Profiler (13km from the coast) and the various ROMS simulations at the mooring site. ROMS = Regional Ocean Modeling System.

surface flow. The cross-shore circulation (see Figure A6d) consists of an offshore flow within the surface Ekman layer ($u < 0$) and a weaker shoreward return flow ($u > 0$) in the subsurface thermocline supported by the equatorward alongshore pressure gradient. This geostrophic current feeds the coastal upwelling (see $w > 0$ in Figure A6c), the CCC, and the PCU. As customary in coastal upwelling systems, an isotherm tilt toward the coast is observed above 100-m depth (see Figure A6a).

Figure A7 and Table A4 display the validation of the mean velocity vertical profile against in situ currents at 30.3°S and 13 km from the coast. The mean model CCC/PCU (Figures A7a and A7b) are comparable with observations in range and structure, although the simulation overestimates/underestimates them because of strong coastal wind forcing. As a typical result in regional oceanic models of the southern HCS (Aguirre et al., 2012, 2014; O. Vergara et al., 2017), the CCC is too energetic overlapping and deepening the PCU (see Figure A6b). As a consequence, the enhanced equatorward pressure gradient forces a shoreward geostrophic current in displacing offshore the surface Ekman current at the coast (see Figure A6d). Indeed Desbiolles et al. (2016) showed that an overestimated coastal wind would impact negatively the structure of the meridional and zonal surface currents and the upwelling dynamics in the EBUS of the Benguela region. They showed that the cross-shore structure of the alongshore winds impact both the offshore and northward surface flows increasing the Ekman transport and the geostrophic adjustment and reducing the intensity and shallowness of the poleward undercurrent.

Table A4
Validation of the Mean Meridional and Zonal Current in the ROMS Experiments Against the Current Meter COSMOS Located at 30.3°S and ~13 km From the Coast

	Meridional current		Zonal current	
ROMS simulation	RMSE (cm s^{-1})	Pearson's correlation	RMSE (cm/s)	Pearson's correlation
CR0	11.5	0.97	3.5	0.61
CR	10.5	0.97	3.6	0.65
DO36	7	0.98	1.6	0.65
DO12	7	0.98	1.6	0.65
DO4	7	0.98	1.6	0.61

Note. RMSE and correlation coefficient are shown. The data were averaged for the available depths between the surface and 100 m. ROMS = Regional Ocean Modeling System; RMSE = Root Mean Square Error.

A2.3. EKE

Nearshore wind-driven currents present strong horizontal and vertical shears. Associated instabilities are the main contributors to the development of mesoscale activity off Central Chile through baroclinic and barotropic energy conversion. Cyclonic eddies populate primarily the CCC, while anticyclonic ones moderately dominate the PCU. This eddy contribution plays an important role in the mean lateral circulation by cross-shore heat flux and depletion of available mean potential energy

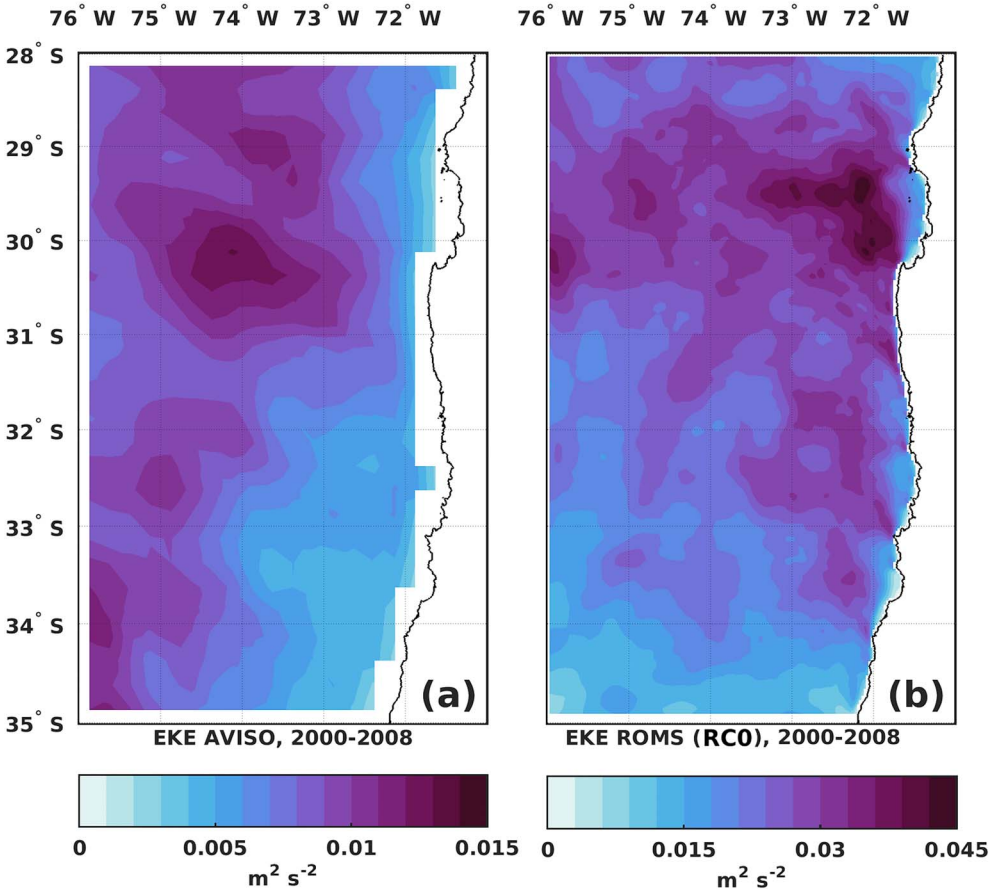

Figure A8. Spatial maps of the temporal mean of the geostrophic surface intraseasonal EKE computed from sea level pressure gradients and derived from (a) AVISO data and from (b) ROMS CR0 over the period (2000–2008). EKE = Eddy Kinetic Energy; Aviso = Archiving, Validation and Interpretation of Satellite Oceanographic; ROMS = Regional Ocean Modeling System.

(Aguirre et al., 2014; Capet et al., 2008; Colas et al., 2012; Hormazabal et al., 2004; Leth & Middleton, 2004; Marchesiello et al., 2003). The mean geostrophic surface intraseasonal EKE, a direct measure of the number and intensity of mesoscale eddy phenomena, was calculated as described in section 2.3.3 for the diagnostic ROMS model (CR0) and compared to satellite estimations (Figure A8). The model spatial pattern of EKE is similar to the one obtained by Aguirre et al. (2014) and in agreement with satellite data. Both observed and simulated fields, Figures A8a and A8b, respectively, present the highest levels of energy (>0.015 m^2/s^2 for AVISO) between 31°S and 28.5°S. However, the simulated EKE range [0–0.045 $m2/s^2$] is broader than the corresponding observed range [0–0.015 $m2/s^2$]. This overestimation was already highlighted in previous studies (Aguirre et al., 2014; Colas et al., 2012; Cambon et al., 2013; O. A. Vergara et al., 2016; O. Vergara et al., 2017) and could be attributed, in part, to a smoothing of the gridded AVISO data. Indeed, we have evidenced a higher agreement in the amplitude range of EKE (not shown) when we use low-pass-filtered (6-day averaging and Gaussian spatial filter with 30-km half-width) ROMS geostrophic velocities, as described in Capet et al. (2008).

Another common feature of the observed and modeled mesoscale activity is a nearshore EKE minimum, in concordance with the idea that EKE originates from instabilities in the nearshore region that amplify while moving offshore (Marchesiello et al., 2003). This assumption is supported in the ROMS solution that evidences a coastal sourcing of EKE around major upwelling regions near Punta Choros (~29°S), Punta Lengua de Vaca (~30°S), and Punta Curaumilla (~33°S), three regions in which atmospheric coastal jets are recurrent. This suggests that mesoscale processes are tied to the coastal topography and local wind forcing. Unfortunately, the AVISO data are not yet reliable in the coastal band to confirm this hypothesis.

Appendix B: Wind Drop-Off Characteristics and Coastal Correction

This appendix provides the details of the method to derive the drop-off length scale and to modify the coastal wind profiles from the WRF model outputs and generate the atmospheric forcing for the sensitivity experiments with ROMS (see Table 2).

B1. Estimate of Wind Drop-Off Characteristics

We follow previous studies that provide estimates of the wind drop-off based either on satellite data (Astudillo et al., 2017) or atmospheric model outputs (Bravo et al., 2016; Renault et al., 2015). The method consists in estimating the distance from the coast, that is, the wind drop-off length (L_d), from which the cross-shore profiles of the magnitude of the wind curl reaches a certain threshold. Here, when applying this wind curl threshold-based methodology, the resulting L_d values were very noisy, exhibiting a large sensitivity to the resolution of the simulated wind that is difficult to interpret all the more so as L_d exhibit already a strong meridional variability (Astudillo et al., 2017). This sensitivity results from the strong aliasing imposed by the bilinear interpolation associated with the upsampling of the WRF wind fields on the high-resolution ROMS grid. Thus, we propose here an alternative approach that provides well-correlated L_d values between the different WRF grid resolutions. First, we estimate within an offshore distance of 150 km the percentage of wind speed reduction (W_r) along the cross-shore profile with respect to its value at the coast as follows:

$$W_r(x,\mathrm{lat}) = \frac{V(x,\mathrm{lat}) - V(0,\mathrm{lat})}{V(x,\mathrm{lat})} \times 100 \tag{B1}$$

where $V(x,\mathrm{lat})$ and $V(0,\mathrm{lat})$ are the model mean wind speed at a given distance x (in meters) from the coast and at the grid point nearest to the coast, respectively (see Figures B1a and B1b). Second, the rate of wind

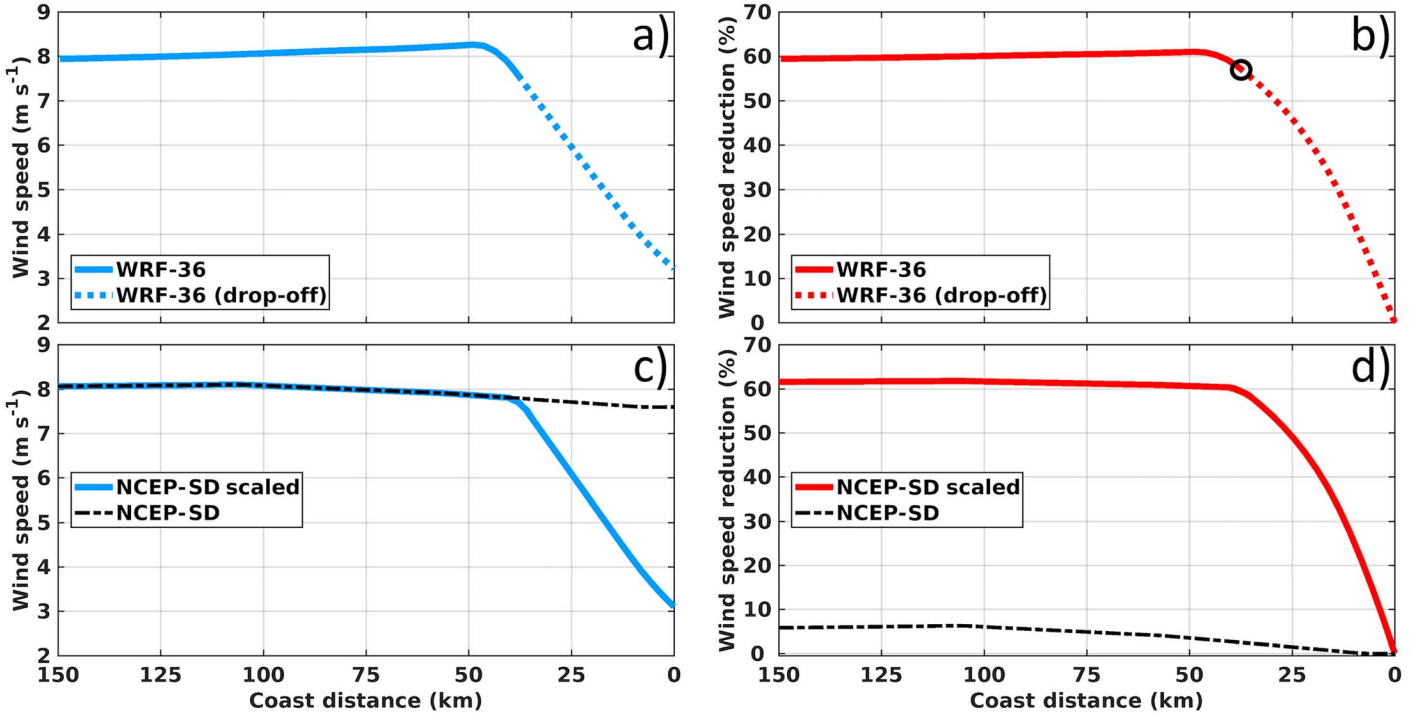

Figure B1. Cross-shore sections of mean alongshore (a) wind speed and (b) percent of wind speed reduction (W_r) at 28.24°S from WRF36 over the period 2007–2008. The black circle and the dotted segments highlight the detected drop-off length (L_d) and the drop-off zone, respectively. (c) Cross-shore section of daily mean (11 October 2008) alongshore wind speed and (d) percent of reduction (W_r) at 28.24°S from NCEP-DS before (black-dashed lines) and after (blue and red lines) the coastal correction. Note how the scaled NCEP-DS wind speed profile starts to mimic the wind drop-off as simulated by the WRF36 domain at a 37.5-km offshore distance from the coast corresponding to the WRF36 wind drop-off length (L_d). WRF = Weather Research and Forecasting; NCEP = National Centers for Environmental Prediction.

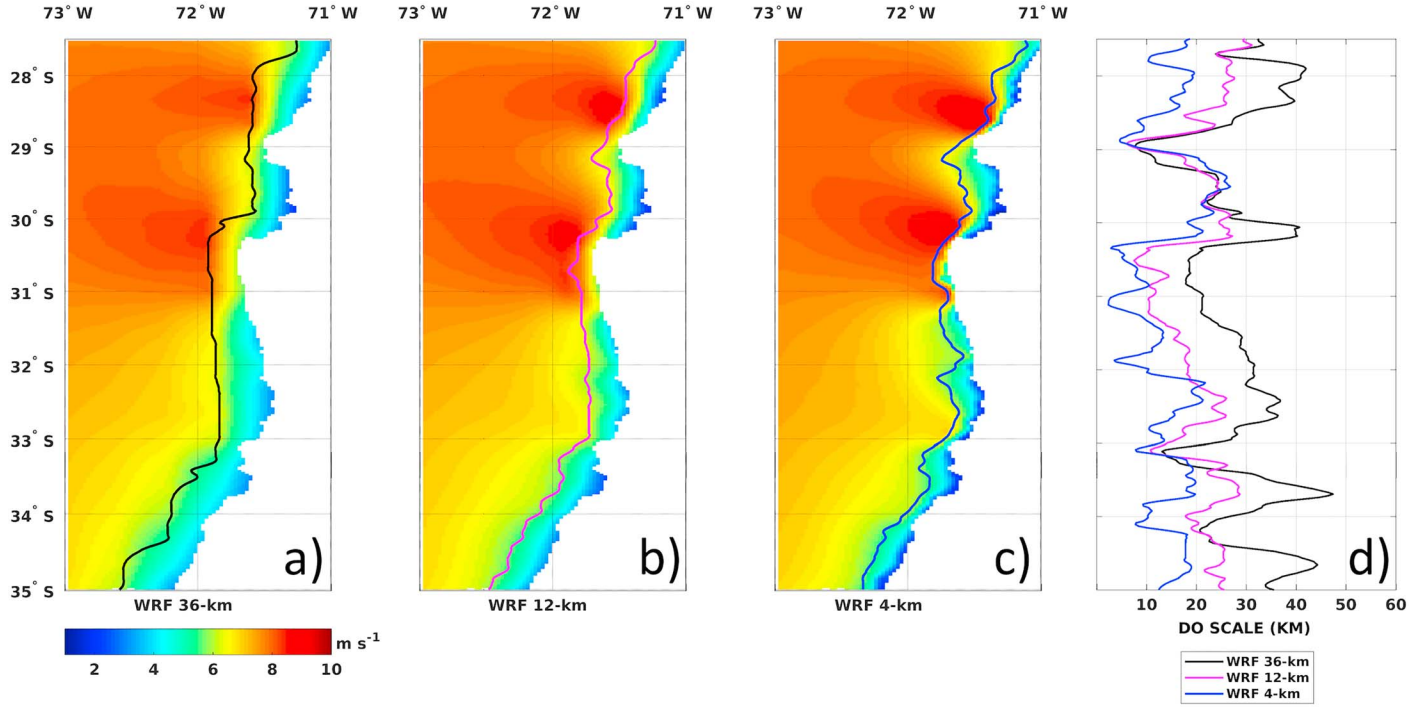

Figure B2. Spatial maps of the temporal mean of the 10-m wind magnitude (m/s) from the triple nest WRF simulation at (a) 36 km, (b) 12 km, and (c) 4 km of spatial resolution over the period 2007–2009. (d) Alongshore wind drop-off length (L_d in km) for the different model resolutions. L_d is estimated by detecting where the cross-shore wind decay rate is >0.5% per kilometer. The black, magenta, and blue lines represent the L_d length for the WRF36, WRF12, and WRF4, respectively. WRF = Weather Research and Forecasting.

decay onshore (growth offshore), corresponding to the slope of W_r at any point x, is approximated using backward differences as

$$\text{wind decay rate} = \frac{\Delta W_r}{\Delta x} \tag{B2}$$

Then, L_d is estimated as the offshore distance where the wind decay rate is greatest than 0.5% per kilometer. This threshold results in a better approximation to the apex of the zonal decay profile W_r that features an exponential shape near the coast. Note that equation (B1) assumes that the zonal profile is an acceptable approximation to the cross-shore one. This is based on the values of the coastline angle for the latitudinal extent (27–35°S) of the oceanic model domain that remains close to 90° (i.e., north-south coastline orientation; see green line in Figure 4 from Dewitte et al., 2008).

B2. Wind Drop-Off Characteristics and Sensitivity to Resolution

Before presenting the method to correct coastal wind profiles in the oceanic model atmospheric forcing, we first document here the latitudinal variability of the wind drop-off in the various atmospheric simulations. Figures B2a–B2c show the mean wind magnitude for each WRF domain; highlighting (color lines) the corresponding wind drop-off scales (Figure B2d). The wind drop-off is present all along the coast with L_d varying from 2 to 50 km depending on the latitude/domain. Furthermore, meridional changes in L_d are associated with orography and coastline geometry. For example, south of the main capes and northwest facing embayments and close to the main upwelling centers (e.g., Punta Choros, ~29°S; Punta Lengua de Vaca, ~30°S; and Punta Curaumilla, ~33°S) small values of L_d are recurrent. In most regions, sensitivity to the spatial resolution is observed: the higher the resolution the smaller the wind drop-off length. Only in some latitudes ranges (e.g., between 29°S and 30°S) the wind drop-off length appears relatively insensitive to the resolution of the model, which could be due to the details in the shape of the coastline and/or orography, as the alternation of promontories and bays (Astudillo et al., 2017; Renault et al., 2015).

B3. Coastal Correction of the Wind Forcing

Our oceanic model experiments are forced using a daily wind data set derived from the statistical downscaling of NCEP1 reanalysis (Kalnay et al., 1996) following the method of Goubanova et al. (2011). This product, hereinafter referred to as NCEP-DS, is based on a multiple linear regression between local/regional variables (predictand) and large-scale climate characteristics (predictors). The predictand is the near-surface wind measured by QuikSCAT scatterometer. The large-scale predictors, covering the QuikSCAT period, are the near-surface wind fields from NCEP1 reanalysis data. The statistical model is applied on wind anomalies relative to a reference mean seasonal cycle that is taken from QuikSCAT data. The statistical relationship between predictand and predictors is then used to downscale NCEP1 winds and provide valuable surface forcing for long-term oceanic regional simulations. Although this technique allows an important correction of the surface wind jet patterns off Central Peru and Central Chile (Goubanova et al., 2011), it cannot overcome the limitations of the QuikSCAT data (i.e., the blind zone). We thus complete the coastal gap in NCEP-DS with the information provided by the WRF simulations at different spatial resolution, to produce atmospheric forcing for the regional oceanic model. Specifically, we apply the wind decay percentages of the mean cross-shore WRF profiles following equation (B1) to the daily NCEP-DS winds along the coast. The NCEP-DS wind magnitude at a distance from the coast equal to the WRF wind drop-off length L_d thus starts to decrease shoreward at a rate similar to the WRF simulation until reaching a low value of wind speed at the closest grid point to the coast. As an illustration, the Figures B1c and B1d present the cross-shore wind profile at 28.24°S for the "raw" NCEP-DS wind and for the "corrected" wind based on the WRF36 simulation.

Acknowledgments

O. Astudillo, B. Dewitte, M. Ramos, F. Frappart, and K. Goubanova acknowledge supports from FONDECYT (projects 1171861 and 1151185) and from (Centre National d'Etudes Spatiales, France) through the OSTST SWANS project. O. Astudillo and J. Rutllant thank the Center for Advanced Studies in Arid Zones (CEAZA), La Serena, Chile for financial support. L. Bravo acknowledge support from CONICYT ("Concurso Nacional Inserción en la Academia, Convocatoria 2016, Folio PAI 79160044"). We thank Abderrahim Bentamy (IFREMER) for valuable discussions. We also would like to thank Catalina Aguirre and an anonymous reviewer for their constructive comments that helped to improve substantially the original manuscript. QSCAT/ASCAT gridded wind data were provided by the CERSAT and are available online at ftp://ftp.ifremer.fr/ifremer/cersat/products/gridded/. Altimetry surface wind intensity was derived from the along-track GDR data provided by the Centre de Topographie des Océans et de l'Hydrosphère (CTOH, Toulouse, France) available at http://ctoh.legos.obs-mip.fr. The MUR/OSTIA SST data are available online at http://podaac.jpl.nasa.gov/dataset/MUR-JPL-L4-GLOB-v4.1 and https://podaac.jpl.nasa.gov/dataset/UKMO-L4HRfnd-GLOB-OSTIA, from the National Aeronautics and Space Administration (NASA) at the Jet Propulsion Laboratory (JPL), California Institute of Technology. The altimeter-derived surface geostrophic currents were obtained at the Globcurrent project (http://globcurrent.ifremer.fr) and provided by AVISO (Archiving, Validation and Interpretation of Satellite Oceanographic data) with support from the French Space Agency (Centre National d'Etudes Spatiales,). In situ Meteo-Oceanographic data are distributed by the monitorig network of the Center for Advanced Studies in Arid Zones (CEAZA) at http://www.ceaza-met.cl. Model outputs analyzed in this article are available upon request to the corresponding author. This work was granted access to the HPC resources of CALMIP supercomputing center under the allocations 2017-1044 and 2018-1044.

References

Aguirre, C., Garreaud, R. D., & Rutllant, J. A. (2014). Surface ocean response to synoptic-scale variability in wind stress and heat fluxes off south-central Chile. *Dynamics of Atmospheres and Oceans*, *65*, 64–85. https://doi.org/10.1016/j.dynatmoce.2013.11.001

Aguirre, C., Pizarro, Ó., Strub, P. T., Garreaud, R., & Barth, J. A. (2012). Seasonal dynamics of the near-surface alongshore flow off central Chile. *Journal of Geophysical Research*, *117*, C01006. https://doi.org/10.1029/2011JC007379

Astudillo, O., Dewitte, B., Mallet, M., Frappart, F., Rutllant, J. A., Ramos, M., et al. (2017). Surface winds off Peru-Chile: Observing closer to the coast from radar altimetry. *Remote Sensing of Environment*, *191*, 179–196. https://doi.org/10.1016/j.rse.2017.01.010

Bakun, A. (1973). Coastal upwelling indices, west coast of North America, 1946-71. U.S. Dept. of Commerce, NOAA Tech. Rep., NMFS SSRF-671 (103p).

Bentamy, A., Croize-Fillon, D., & Perigaud, C. (2008). Characterization of ASCAT measurements based on buoy and QuikSCAT wind vector observations. *Ocean Science*, *4*(4), 265–274. https://doi.org/10.5194/os-4-265-2008

Bentamy, A., & Fillon, D. C. (2012). Gridded surface wind fields from Metop/ASCAT measurements. *International Journal of Remote Sensing*, *33*(6), 1729–1754. https://doi.org/10.1080/01431161.2011.600348

Blanco, J. L., Thomas, A. C., Carr, M.-E., & Strub, P. T. (2001). Seasonal climatology of hydrographic conditions in the upwelling region off northern Chile. *Journal of Geophysical Research*, *106*(C6), 11451–11467. https://doi.org/10.1029/2000JC000540

Boé, J., Hall, A., Colas, F., McWilliams, J. C., Qu, X., Kurian, J., & Kapnick, S. B. (2011). What shapes mesoscale wind anomalies in coastal upwelling zones? *Climate Dynamics*, *36*(11–12), 2037–2049. https://doi.org/10.1007/s00382-011-1058-5

Bravo, L., Ramos, M., Astudillo, O., Dewitte, B., & Goubanova, K. (2016). Seasonal variability of the Ekman transport and pumping in the upwelling system off central-northern Chile (30°S) based on a high-resolution atmospheric regional model (WRF). *Ocean Science*, *12*(5), 1049–1065. https://doi.org/10.5194/os-12-1049-2016

Cambon, G., Goubanova, K., Marchesiello, P., Dewitte, B., Illig, S., & Echevin, V. (2013). Assessing the impact of downscaled winds on a regional ocean model simulation of the Humboldt system. *Ocean Modelling*, *65*, 11–24. https://doi.org/10.1016/j.ocemod.2013.01.007

Capet, X., Colas, F., McWilliams, J. C., Penven, P., & Marchesiello, P. (2008). Eddies in eastern boundary subtropical upwelling systems. In *Ocean modeling in an eddying regime*. [On-line, (pp. 131–147). Washington, D. C: American Geophysical Union. https://doi.org/10.1029/177gm10

Capet, X., Estrade, P., Machu, E., Ndoye, S., Grelet, J., Lazar, A., et al. (2017). On the dynamics of the Southern Senegal upwelling center: Observed variability from synoptic to superinertial scales. *Journal of Physical Oceanography*, *47*(1), 155–180. https://doi.org/10.1175/JPO-D-15-0247.1

Capet, X. J., Marchesiello, P., & McWilliams, J. C. (2004). Upwelling response to coastal wind profiles. *Geophysical Research Letters*, *31*, L13311. https://doi.org/10.1029/2004GL020123

Carr, M.-E., & Kearns, E. J. (2003). Production regimes in four Eastern boundary current systems. *Deep Sea Research Part II: Topical Studies in Oceanography*, *50*(22–26), 3199–3221. https://doi.org/10.1016/j.dsr2.2003.07.015

Carton, J. A., & Giese, B. S. (2008). A reanalysis of ocean climate using simple ocean data assimilation (SODA). *Monthly Weather Review*, *136*(8), 2999–3017. https://doi.org/10.1175/2007MWR1978.1

Chavez, F. P., & Messié, M. (2009). A comparison of Eastern boundary upwelling ecosystems. *Progress in Oceanography*, *83*(1–4), 80–96. https://doi.org/10.1016/j.pocean.2009.07.032

Chin, T. M., Milliff, R. F., & Large, W. G. (1998). Basin-scale, high-wavenumber sea surface wind fields from a multiresolution analysis of scatterometer data. *Journal of Atmospheric and Oceanic Technology*, *15*(3), 741–763. https://doi.org/10.1175/1520-0426(1998)015<0741:BSHWSS>2.0.CO;2

Colas, F., McWilliams, J. C., Capet, X., & Kurian, J. (2012). Heat balance and eddies in the Peru-Chile current system. *Climate Dynamics*, *39*(1–2), 509–529. https://doi.org/10.1007/s00382-011-1170-6

Croquette, M., Eldin, G., Grados, C., & Tamayo, M. (2007). On differences in satellite wind products and their effects in estimating coastal upwelling processes in the South-East Pacific. *Geophysical Research Letters*, *34*, L22301. https://doi.org/10.1029/2006GL027538

da Silva, A. M., Young-Molling, C. C., & Levitus, S. (Eds) (1994). Atlas of surface marine data 1994, Volume 1. In *Algorithms and Procedures, NOAA Atlas NESDIS*, (Vol. 6, p. 83). Silver Spring, Md: NOAA.

Demarcq, H. (2009). Trends in primary production, sea surface temperature and wind in upwelling systems (1998–2007). *Progress in Oceanography*, *83*(1–4), 376–385. https://doi.org/10.1016/j.pocean.2009.07.022

Desbiolles, F., Blanke, B., Bentamy, A., & Roy, C. (2016). Response of the Southern Benguela upwelling system to fine-scale modifications of the coastal wind. *Journal of Marine Systems*, *156*, 46–55. https://doi.org/10.1016/j.jmarsys.2015.12.002

Dewitte, B., Ramos, M., Echevin, V., Pizarro, O., & duPenhoat, Y. (2008). Vertical structure variability in a seasonal simulation of a medium-resolution regional model of the Eastern South Pacific. *Progress in Oceanography*, *79*(2–4), 120–137. https://doi.org/10.1016/j.pocean.2008.10.014

Dewitte, B., Vazquez-Cuervo, J., Goubanova, K., Illig, S., Takahashi, K., Cambon, G., et al. (2012). Change in El Niño flavours over 1958–2008: Implications for the long-term trend of the upwelling off Peru. *Deep Sea Research Part II: Topical Studies in Oceanography*, *77-80*, 143–156. https://doi.org/10.1016/j.dsr2.2012.04.011

Di Lorenzo, E. (2003). Seasonal dynamics of the surface circulation in the Southern California current system. *Deep Sea Research Part II: Topical Studies in Oceanography*, *50*(14–16), 2371–2388. https://doi.org/10.1016/S0967-0645(03)00125-5

Donlon, C. J., Martin, M., Stark, J., Roberts-Jones, J., Fiedler, E., & Wimmer, W. (2012). The operational sea surface temperature and sea ice analysis (OSTIA) system. *Remote Sensing of Environment*, *116*, 140–158. https://doi.org/10.1016/j.rse.2010.10.017

Dorman, C. E., Dever, E. P., Largier, J., & Koračin, D. (2006). Buoy measured wind, wind stress and wind stress curl over the shelf off Bodega Bay, California. *Deep Sea Research Part II: Topical Studies in Oceanography*, *53*(25–26), 2850–2864. https://doi.org/10.1016/j.dsr2.2006.07.006

Dufois, F., Penven, P., Peter Whittle, C., & Veitch, J. (2012). On the warm nearshore bias in Pathfinder monthly SST products over Eastern boundary upwelling systems. *Ocean Modelling*, *47*, 113–118. https://doi.org/10.1016/j.ocemod.2012.01.007

Edwards, K. A., Rogerson, A. M., Winant, C. D., & Rogers, D. P. (2001). Adjustment of the marine atmospheric boundary layer to a coastal cape. *Journal of the Atmospheric Sciences*, *58*(12), 1511–1528. https://doi.org/10.1175/1520-0469(2001)058<1511:AOTMAB>2.0.CO;2

Escribano, R., & Schneider, W. (2007). The structure and functioning of the coastal upwelling system off central/southern Chile. *Progress in Oceanography*, *75*(3), 343–347. https://doi.org/10.1016/j.pocean.2007.08.020

Estrade, P., Marchesiello, P., De Verdière, A. C., & Roy, C. (2008). Cross-shelf structure of coastal upwelling: A two-dimensional extension of Ekman's theory and a mechanism for inner shelf upwelling shut down. *Journal of Marine Research. Journal of Marine Research/Yale*, *66*(5), 589–616. https://doi.org/10.1357/002224008787536790

Fairall, C. W., Bradley, E. F., Hare, J. E., Grachev, A. A., & Edson, J. B. (2003). Bulk parametrization of air–sea fluxes: Updates and verification for the COARE algorithm. *Journal of Climate*, *16*(4), 571–591. https://doi.org/10.1175/1520-0442(2003)016<0571:BPOASF>2.0.CO;2

Garreaud, R., & Muñoz, R. C. (2005). The low-level jet off the West Coast of subtropical South America: Structure and variability. *Monthly Weather Review*, *133*(8), 2246–2261. https://doi.org/10.1175/mwr2972.1

Garreaud, R., & Rutllant, J. (2003). Coastal lows along the subtropical West Coast of South America: Numerical simulation of a typical case. *Monthly Weather Review*, *131*(5), 891–908. https://doi.org/10.1175/1520-0493(2003)131<0891:CLATSW>2.0.CO;2

Garreaud, R. D., Rutllant, J. A., Muñoz, R. C., Rahn, D. A., Ramos, M., & Figueroa, D. (2011). VOCALS-: the Chilean upwelling experiment. *Atmospheric Chemistry and Physics*, *11*(5), 2015–2029. https://doi.org/10.5194/acp-11-2015-2011

Gill, A. (1982). *Atmosphere-ocean dynamics*. New York: Academic Press.

Goubanova, K., Echevin, V., Dewitte, B., Codron, F., Takahashi, K., Terray, P., & Vrac, M. (2011). Statistical downscaling of sea-surface wind over the Peru–Chile upwelling region: Diagnosing the impact of climate change from the IPSL-CM4 model. *Climate Dynamics*, *36*(7–8), 1365–1378. https://doi.org/10.1007/s00382-010-0824-0

Gruber, N., Frenzel, H., Doney, S. C., Marchesiello, P., McWilliams, J. C., Moisan, J. R., et al. (2006). Eddy-resolving simulation of plankton ecosystem dynamics in the California Current System. *Deep Sea Research Part I: Oceanographic Research Papers*, *53*(9), 1483–1516. https://doi.org/10.1016/j.dsr.2006.06.005

Gruber, N., Lachkar, Z., Frenzel, H., Marchesiello, P., Münnich, M., McWilliams, J. C., et al. (2011). Eddy-induced reduction of biological production in eastern boundary upwelling systems. *Nature Geoscience*, *4*(11), 787–792. https://doi.org/10.1038/NGEO1273

Halpern, D. (2002). Offshore Ekman transport and Ekman pumping off Peru during the 1997–1998 El Niño. *Geophysical Research Letters*, *29*(5), 1075. https://doi.org/10.1029/2001GL014097

Hong, X., Wang, S., Holt, T. R., Martin, P. J., & O'Neill, L. (2013). Modulation of the sea-surface temperature in the Southeast Pacific by the atmospheric low-level coastal jet. *Journal of Geophysical Research: Oceans*, *118*, 3979–3998. https://doi.org/10.1002/jgrc.20289

Hormazabal, S., Shaffer, G., & Leth, O. (2004). Coastal transition zone off Chile. *Journal of Geophysical Research*, *109*, C01021. https://doi.org/10.1029/2003JC001956

Illig, S., Dewitte, B., Goubanova, K., Cambon, G., Boucharel, J., Monetti, F., et al. (2014). Forcing mechanisms of intraseasonal SST variability off central Peru in 2000–2008. *Journal of Geophysical Research: Oceans*, *119*, 3548–3573. https://doi.org/10.1002/2013JC009779

Kalnay, E., Kanamitsu, M., Kistler, R., Collins, W., Deaven, D., Gandin, L., et al. (1996). The NCEP/NCAR 40-year reanalysis project. *Bulletin of the American Meteorological Society*, *77*(3), 437–471. https://doi.org/10.1175/15200477(1996)077<0437:TNYRP>2.0.CO;2

Large, W. G., McWilliams, J. C., & Doney, S. C. (1994). Oceanic vertical mixing: A review and a model with a nonlocal boundary layer parametrization. *Reviews of Geophysics*, *32*(4), 363. https://doi.org/10.1029/94RG01872

Leth, O., & Middleton, J. F. (2004). A mechanism for enhanced upwelling off central Chile: Eddy advection. *Journal of Geophysical Research*, *109*, C12020. https://doi.org/10.1029/2003JC002129

Marchesiello, P., & Estrade, P. (2010). Upwelling limitation by onshore geostrophic flow. *Journal of Marine Research. Journal of Marine Research/Yale*, *68*(1), 37–62. https://doi.org/10.1357/002224010793079004

Marchesiello, P., McWilliams, J. C., & Shchepetkin, A. (2003). Equilibrium structure and dynamics of the California Current System. *Journal of Physical Oceanography*, *33*(4), 753–783. https://doi.org/10.1175/1520-0485(2003)33<753:esadot>2.0.co;2

Mason, E., Colas, F., Molemaker, J., Shchepetkin, A. F., Troupin, C., McWilliams, J. C., & Sangrà, P. (2011). Seasonal variability of the Canary Current: A numerical study. *Journal of Geophysical Research*, *116*, C06001. https://doi.org/10.1029/2010JC006665

Mason, E., Molemaker, J., Shchepetkin, A. F., Colas, F., McWilliams, J. C., & Sangrà, P. (2010). Procedures for off-line grid nesting in regional ocean models. *Ocean Modelling*, *35*(1–2), 1–15. https://doi.org/10.1016/j.ocemod.2010.05.007

Montes, I., Colas, F., Capet, X., & Schneider, W. (2010). On the pathways of the equatorial subsurface currents in the eastern equatorial Pacific and their contributions to the Peru-Chile undercurrent. *Journal of Geophysical Research*, *115*, C09003. https://doi.org/10.1029/2009JC005710

Oerder, V., Colas, F., Echevin, V., Masson, S., Hourdin, C., Jullien, S., et al. (2016). Mesoscale SST–wind stress coupling in the Peru–Chile current system: Which mechanisms drive its seasonal variability? *Climate Dynamics*, *47*(7–8), 2309–2330. https://doi.org/10.1007/s00382-015-2965-7

Paulson, C. A., & Simpson, J. J. (1977). Irradiance measurements in the upper ocean. *Journal of Physical Oceanography*, *7*(6), 952–956. https://doi.org/10.1175/1520-0485(1977)007<0952:IMITUO>2.0.CO;2

Penven, P., Echevin, V., Pasapera, J., Colas, F., & Tam, J. (2005). Average circulation, seasonal cycle, and mesoscale dynamics of the Peru Current System: A modeling approach. *Journal of Geophysical Research*, *110*, C10021. https://doi.org/10.1029/2005JC002945

Penven, P., Roy, C., Lutjeharms, J. R. E., Colin de Verdière, A., Johnson, A., Shillington, F., et al. (2001). A regional hydrodynamic model of the Southern Benguela. *South African Journal of Science*, *97*, 472–476.

Perlin, N., Skyllingstad, E. D., Samelson, R. M., & Barbour, P. L. (2007). Numerical simulation of air–sea coupling during coastal upwelling. *Journal of Physical Oceanography*, *37*(8), 2081–2093. https://doi.org/10.1175/JPO3104.1

Pickett, M. H., & Paduan, J. D. (2003). Ekman transport and pumping in the California Current based on the U.S. Navy's high-resolution atmospheric model (COAMPS). *Journal of Geophysical Research*, *108*(C10), 3327. https://doi.org/10.1029/2003JC001902

Rahn, D. A., & Garreaud, R. D. (2013). A synoptic climatology of the near-surface wind along the west coast of South America. *International Journal of Climatology*, *34*(3), 780–792. https://doi.org/10.1002/joc.3724

Rahn, D. A., Garreaud, R. D., & Rutllant, J. A. (2011). The low-level atmospheric circulation near Tongoy Bay–Point Lengua de Vaca (Chilean Coast, 30°S). *Monthly Weather Review*, *139*(11), 3628–3647. https://doi.org/10.1175/MWR-D-11-00059.1

Renault, L., Deutsch, C., McWilliams, J. C., Frenzel, H., Liang, J.-H., & Colas, F. (2016). Partial decoupling of primary productivity from upwelling in the California Current system. *Nature Geoscience*, *9*(7), 505–508. https://doi.org/10.1038/ngeo2722

Renault, L., Dewitte, B., Marchesiello, P., Illig, S., Echevin, V., Cambon, G., et al. (2012). Upwelling response to atmospheric coastal jets off central Chile: A modeling study of the October 2000 event. *Journal of Geophysical Research*, *117*, C02030. https://doi.org/10.1029/2011JC007446

Renault, L., Hall, A., & McWilliams, J. C. (2015). Orographic shaping of US West Coast wind profiles during the upwelling season. *Climate Dynamics*, *46*(1–2), 273–289. https://doi.org/10.1007/s00382-015-2583-4

Renault, L., Molemaker, M. J., McWilliams, J. C., Shchepetkin, A. F., Lemarié, F., Chelton, D., et al. (2016). Modulation of wind work by oceanic current interaction with the atmosphere. *Journal of Physical Oceanography*, *46*(6), 1685–1704. https://doi.org/10.1175/JPO-D-15-0232.1

Ridgway, K. R., Dunn, J. R., & Wilkin, J. L. (2002). Ocean interpolation by four-dimensional weighted least squares—Application to the waters around Australasia. *Journal of Atmospheric and Oceanic Technology*, *19*(9), 1357–1375. https://doi.org/10.1175/1520-0426(2002)019<1357:OIBFDW>2.0.CO;2

Rio, M.-H., Mulet, S., & Picot, N. (2014). Beyond GOCE for the ocean circulation estimate: Synergetic use of altimetry, gravimetry, and in situ data provides new insight into geostrophic and Ekman currents. *Geophysical Research Letters*, *41*, 8918–8925. https://doi.org/10.1002/2014gl061773

Rutllant, J. A., Masotti, I., Calderón, J., & Vega, S. A. (2004). A comparison of spring coastal upwelling off central Chile at the extremes of the 1996–1997 ENSO cycle. *Continental Shelf Research*, *24*(7–8), 773–787. https://doi.org/10.1016/j.csr.2004.02.005

Scaff, L., Rutllant, J. A., Rahn, D., Gascoin, S., & Rondanelli, R. (2017). Meteorological interpretation of orographic precipitation gradients along an Andes West Slope Basin at 30°S (Elqui Valley, Chile). *Journal of Hydrometeorology*, *18*(3), 713–727. https://doi.org/10.1175/JHM-D-16-0073.1

Send, U. (1989). The origin of eddy heat fluxes in the northern California upwelling regime. *Journal of Geophysical Research*, *94*(C1), 871. https://doi.org/10.1029/JC094iC01p00871

Shchepetkin, A. F., & McWilliams, J. C. (2005). The regional oceanic modeling system (ROMS): A split-explicit, free-surface, topography-following-coordinate oceanic model. *Ocean Modelling*, *9*(4), 347–404. https://doi.org/10.1016/j.ocemod.2004.08.002

Shchepetkin, A. F., & McWilliams, J. C. (2009). Correction and commentary for "Ocean forecasting in terrain-following coordinates: Formulation and skill assessment of the regional ocean modeling system" by Haidvogel et al., J. Comp. Phys. 227, pp. 3595–3624. *Journal of Computational Physics*, *228*(24), 8985–9000. https://doi.org/10.1016/j.jcp.2009.09.002

Skamarock, W. C., & Klemp, J. B. (2008). A time-split nonhydrostatic atmospheric model for weather research and forecasting applications. *Journal of Computational Physics*, *227*(7), 3465–3485. https://doi.org/10.1016/j.jcp.2007.01.037

Smith, R. L. (1968). Upwelling. *Oceanography and Marine Biology: An Annual Review*, *6*, 11–46.

Smith, R. L. (1995). The physical processes of coastal ocean upwelling systems. In C. P. Summerhayes, et al. (Eds.), *Upwelling in the ocean: Modern processes and ancient records*, (pp. 39–64). Hoboken, N. J: John Wiley.

Stark JD, Donlon CJ, Martin MJ and McCulloch ME (2007). OSTIA: An operational, high resolution, real time, global sea surface temperature analysis system. OCEANS 2007 - Europe. paper presented at the OCEANS 2007 - Europe. IEEE. https://doi.org/10.1109/OCEANSE.2007.4302251

Stiles, B. (2014). Discovering a decade of coastal winds from scatterometers, IOVWST (International Ocean Vector Winds Science Team) meeting sponsored by NASA, FSU, COAP, EUMETSAT, , ESA and Ifremer, Brest, France, 2–4 June.

Veitch, J., Penven, P., & Shillington, F. (2010). Modeling equilibrium dynamics of the Benguela Current System. *Journal of Physical Oceanography*, *40*(9), 1942–1964. https://doi.org/10.1175/2010JPO4382.1

Vergara, O., Dewitte, B., Ramos, M., & Pizarro, O. (2017). Vertical energy flux at ENSO time scales in the subthermocline of the Southeastern Pacific. *Journal of Geophysical Research: Oceans*, *122*, 6011–6038. Http://dx.doi.org/10.1002/2016JC012614

Vergara, O., Dewitte, B., Montes, I., Garçon, V., Ramos, M., Paulmier, A., & Pizarro, O. (2016). Seasonal variability of the oxygen minimum zone off Peru in a high-resolution regional coupled model. *Biogeosciences*, *13*(15), 4389–4410. https://doi.org/10.5194/bg-13-4389-2016

Vergara, O. A., Echevín, V., Sepúlveda, H. H., Colas, F., & Quiñones, R. A. (2016). Modelling the seasonal dynamics of the Peru-Chile undercurrent off Central Chile (30–40°S). *Continental Shelf Research*, *123*, 61–79. https://doi.org/10.1016/j.csr.2016.04.001

Verhoef, A., Stoffelen, A., (2013). Validation of ASCAT coastal winds, Version 1.5 Document External Project: 2013, SAF/OSI/CDOP/KNMI/TEC/RP/176, EUMETSAT.

Vogelzang, J., Stoffelen, A., Verhoef, A., & Figa-Saldaña, J. (2011). On the quality of high-resolution scatterometer winds. *Journal of Geophysical Research*, *116*, C10033. https://doi.org/10.1029/2010JC006640

vonStorch, H., & Zwiers, F. W. (1999). *Statistical analysis in climate research*, (p. 494). Cambrigde, UK: Cambridge Univ. Press.

Wang, D., Gouhier, T. C., Menge, B. A., & Ganguly, A. R. (2015). Intensification and spatial homogenization of coastal upwelling under climate change. *Nature*, *518*(7539), 390–394. https://doi.org/10.1038/nature14235

Yang, J. (2006). The seasonal variability of the Arctic Ocean Ekman transport and its role in the mixed layer heat and salt fluxes. *Journal of Climate*, *19*(20), 5366–5387. https://doi.org/10.1175/JCLI3892.1